


December 2020

Characterization of Fiber Bragg Grating Based, Geometry-dependent, Magnetostrictive Composite Sensors

Edward Lynch
University of Wisconsin-Milwaukee

Follow this and additional works at: <https://dc.uwm.edu/etd>

 Part of the [Electrical and Electronics Commons](#), [Materials Science and Engineering Commons](#), and the [Optics Commons](#)

Recommended Citation

Lynch, Edward, "Characterization of Fiber Bragg Grating Based, Geometry-dependent, Magnetostrictive Composite Sensors" (2020). *Theses and Dissertations*. 2556.
<https://dc.uwm.edu/etd/2556>

This Thesis is brought to you for free and open access by UWM Digital Commons. It has been accepted for inclusion in Theses and Dissertations by an authorized administrator of UWM Digital Commons. For more information, please contact open-access@uwm.edu.

CHARACTERIZATION OF
FIBER BRAGG GRATING BASED, GEOMETRY-DEPENDENT,
MAGNETOSTRICTIVE COMPOSITE SENSORS

by

Edward Lynch

A Thesis Submitted in
Partial Fulfillment of the
Requirements for the Degree of

Master of Science
in Engineering

at

The University of Wisconsin-Milwaukee

December 2020

ABSTRACT

CHARACTERIZATION OF FIBER BRAGG GRATING BASED, GEOMETRY-DEPENDENT, MAGNETOSTRICTIVE COMPOSITE SENSORS

by

Edward Lynch

The University of Wisconsin-Milwaukee, 2020
Under the Supervision of Professor Chiu Tai Law

Optical sensors based on geometry dependent magnetostrictive composite, having potential applications in current sensing and magnetic field sensing are modeled and evaluated experimentally with an emphasis on their thermal immunity from thermal disturbances. Two sensor geometries composed of a fiber Bragg grating (FBG) embedded in a shaped Terfenol-D/epoxy composite material, which were previously prototyped and tested for magnetic field response, were investigated. When sensing magnetic fields or currents, the primary function of the magnetostrictive composite geometry is to modulate the magnetic flux such that a magnetostrictive strain gradient is induced on the embedded FBG. Simulations and thermal experiments reveal the thermal limitations and geometry dependence of the sensors. Also, during the course of this study, new insights into the effects of environmental factors and sensor manufacturing techniques were uncovered which warrant further investigation.

© Copyright by Edward Lynch, 2020
All Rights Reserved

TABLE OF CONTENTS

List of Figures.....	vi
List of Tables.....	ix
List of Abbreviations.....	x
Acknowledgements.....	xii
1 Introduction.....	1
1.1 Background.....	1
1.2 Thesis Objective.....	3
1.3 Thesis Structure.....	4
2 Theory.....	5
2.1 Mechanical Deformation.....	5
2.2 Magnetostriction.....	6
2.3 Fiber Bragg Grating.....	10
2.4 Thermal Expansion.....	12
2.5 Moisture Expansion.....	12
2.6 SLED.....	13
2.7 Heat Transfer.....	13
3 Computational Modeling.....	15
3.1 Octave Modeling.....	15
3.2 Comsol Modeling.....	16
3.2.1 Composite Curing.....	16
3.2.2 Magnetostriction.....	17
3.2.3 Thermal Expansion.....	19
4 Sensor Manufacturing.....	22
5 Experimental Methods.....	27
5.1 Optical Design.....	27

5.2 Thermal Chamber.....	29
5.2.1 Thermal Chamber Design.....	30
5.2.2 Thermal Chamber Experiments.....	34
5.2.3 Thermal Chamber Data Analysis.....	35
5.3 Water Bath.....	41
5.3.1 Water Bath Design.....	42
5.3.2 Water Bath Experiments.....	46
5.3.3 Water Bath Data Analysis.....	49
6 Conclusion.....	62
7 Future Work.....	65
Bibliography.....	67

LIST OF FIGURES

Figure 1: Magnetostriction, where H is applied magnetic field strength and Δl is the change in length of the material.....	7
Figure 2: Fiber Bragg grating with uniform grating Λ , where n_1 , n_2 , and n_3 correspond to the core, cladding, and FBG grating refractive indices.....	10
Figure 3: Chirped fiber Bragg grating with non-uniform grating period.....	11
Figure 4: Fiber Bragg grating Gaussian apodization.....	11
Figure 5: Comsol model B-H curve 27% composite volume fraction.....	18
Figure 6: Simulated trapezoidal sensor FBG optical response computed from resulting strain found in Comsol using new B-H curve and post processed using Octave scripting.....	19
Figure 7: Simulated normalized trapezoidal slab reflected spectral power after adjusting LCTE in Comsol model.....	20
Figure 8: Trapezoidal slab normalized simulated reflected power.....	21
Figure 9: Trapezoidal slab.....	24
Figure 10: Acute Saccharin quadrilateral slab.....	24
Figure 11: Magnetostrictive composite slab molding setup.....	26
Figure 12: Computer controlled optical attenuator.....	29
Figure 13: Thermal chamber front view (left) and rear view (right).....	30
Figure 14: Thermal chamber (inside view) air flow components.....	31
Figure 15: Thermal chamber (inside view) heating element, IR shield, and temperature sensor. .	31
Figure 16: Thermal chamber electrical block diagram.....	33
Figure 17: Thermal chamber experimental setup.....	34
Figure 18: Thermal chamber experimental results - SLED output power measured in terms of photodetector voltage with a 3.8k load resistor.....	37

Figure 19: Thermal chamber experimental results - trapezoidal slab sensor reflected optical power based on integration of OSA spectrum.....	38
Figure 20: Thermal chamber experimental results - normalized sensor and SLED optical power for data in Figures 18 and 19.....	39
Figure 21: Thermal chamber experimental results - normalized sensor returned optical power for trapezoidal slab sensor in Figure 18 adjusted for SLED fluctuations with temperature in Figure 19.....	40
Figure 22: Thermal chamber experimental results - SLED power compensated normalized sensor reflected optical power at steady state temperature for trapezoidal slab.....	41
Figure 23: Water bath thermal experiment apparatus (top view).....	43
Figure 24: Custom TEC water bath cooler.....	45
Figure 25: Custom TEC block diagram.....	46
Figure 26: Water bath experimental setup.....	46
Figure 27: Water bath PVC vessel sensor placement: A) trapezoidal slab 0°, B) trapezoidal slab 90°, C) acute Saccharin quadrilateral 0°, D) acute Saccharin quadrilateral 90°.....	48
Figure 28: Water bath experimental results - temperature.....	54
Figure 29: Water bath experimental results - SLED output power measured in terms of photodetector voltage with a 3.8k load resistor - fixed sample time (cubic interpolation).....	55
Figure 30: Water bath experimental results - normalized SLED optical power for data in Figure 29.....	56
Figure 31: Water bath experimental results - sensor reflected optical power based on integration of OSA spectrum - fixed sample time (cubic interpolation).....	57
Figure 32: Water bath experimental results - normalized sensor reflected optical power for data in Figure 31.....	58
Figure 33: Water bath experimental results - normalized sensor reflected optical power in Figure 32 adjusted for SLED fluctuations with temperature in Figure 30.....	59

Figure 34: Water bath experimental results - source adjusted normalized sensor reflected optical power in Figure 33 with 10 minute moving average filter applied.....60

Figure 35: Water bath experimental results - sensor reflected optical power (last 30 minutes hold time average, normalized to 20°C) vs temperature.....61

LIST OF TABLES

Table 1: SLED parameters @ T=20°C, I=500mA.....	13
Table 2: Trapezoidal slab dimensions.....	25
Table 3: Acute Saccharin quadrilateral slab dimensions.....	25
Table 4: Water bath experiment plot naming convention.....	50
Table 5: Data alignment time offset and coupling coefficients calculated using linear regression method.....	52

LIST OF ABBREVIATIONS

A/D	-	Analog to Digital
ABB	-	Formerly ASEA Brown Boveri (Company Name)
AC	-	Alternating Current
ANSI	-	American National Standards Institute
B-H	-	Magnetic Flux Density - Magnetic Field Strength
CME	-	Coefficient of Moisture Expansion
CPU	-	Central Processing Unit
CSV	-	Comma Separated Value (file format)
D/A	-	Digital to Analog
DAQ	-	Data Acquisition
DC	-	Direct Current
EXP	-	Experiment
FBG	-	Fiber Bragg Grating
FMIN	-	Python 'scipy.optimize.fmin' Library Function
HMA	-	Hot Melt Adhesive
HV	-	High Voltage
IR	-	Infra-Red Radiation
LCTE	-	Linear Coefficient of Thermal Expansion
LP	-	Low Pass
M-H	-	Material Magnetization - Magnetic Field Strength
MATLAB	-	Computational Computing and Modeling Software
MOSFET	-	Metal–Oxide–Semiconductor Field-Effect Transistor
MV	-	Medium Voltage
NI	-	National Instruments

OSA	-	Optical Spectrum Analyzer
PI	-	Proportional Integral
PVC	-	Polyvinyl Chloride (Synthetic Plastic)
RTD	-	Resistance Temperature Detector
SLED	-	Superluminescent Light Emitting Diode
TEC	-	Thermoelectric Cooler
USB	-	Universal Serial Bus
UWM	-	University of Wisconsin – Milwaukee
λ -H	-	Magnetostrictive Strain - Magnetic Field Strength

ACKNOWLEDGEMENTS

I would like to thank my advisor Dr. Chiu Law. I appreciate all of the help, support, and guidance you have given me over the years. If it weren't for your patience and encouragement, I would not have come this far.

I would like to thank Dr. Rani Elhajjar for the insights into composite materials and how to model them in Comsol. I would also like to thank you for the use of your lab and specialized equipment.

I would like to thank Suha Lasassmeh, David Frailey, Aaron Mueller, and Ashraf Al-Hajjeh, whose previous works, collaborations, and insights helped further the development and knowledge base of magnetostrictive composites and optics for use in sensing applications.

Finally, I would like to thank all of the other great professors I've had the pleasure of learning from during my time at the University of Wisconsin - Milwaukee.

Chapter 1

1 Introduction

1.1 Background

Traditionally, current sensors have been either resistive based (Ohm's Law), inductive based (Faraday's Law), or magnetic field sensor based. The most widely used resistive based current sensor is the shunt resistor, which can be used in both alternating current (AC) and direct current (DC) sensing. Current transformers and Rogowski coils are two of the most commonly used types of inductive based current sensors, having the limitation of only being able to measure AC. Hall effect based current sensors are the most common magnetic field based current sensors and can be used to sense both alternating current (AC) and direct current (DC).

When designing a sensing system, especially for medium voltage (MV) and high voltage (HV) systems, American National Standards Institute (ANSI) C84.1-1989 [1], whether for controls or monitoring purposes, electrical isolation between high voltage components and sensing/control components is an essential consideration. When it comes to electrical isolation, the traditional methods of current sensing all require electrical wirings to be made in the vicinity of the high voltage conductors. If the electrical isolation between the sensing device and the wires used to connect to the sensor breaks down, especially in MV and HV applications, a hazardous situation could arise. High voltage sensing dangers include risks of short circuit, common mode and differential mode interference, damage to sensing equipment, etc.

Optical isolation is one way to mitigate the safety issues that arise when sensing currents in MV and HV applications. The higher the voltage, the more difficult the problem of isolation becomes. Optical data transmission circuits are one way to accomplish electrical isolation between sensor and circuit under test; however, these can be disadvantageous in cost and complexity, depending on the voltage isolation required.

More recently, optical current sensing techniques have been developed which allow for electrically isolated current measurements that do not require optical data transmission circuits, but instead rely on the measurement of light passed through or reflected within optical fibers. One such technique is based on the magneto-optical phenomenon, known as the Faraday effect, in which the polarization of light traveling through an optical fiber changes in the presence of a magnetic field, discussed in Aerssens et al. [2] and demonstrated commercially by ABB [3]. An even more recent technique is based on magnetostriction, the property in which a ferromagnetic material deforms in the presence of a magnetic field in conjunction with optical communications components known as fiber Bragg gratings (FBGs).

The University of Wisconsin – Milwaukee (UWM) has been in the process of developing a geometry dependent magnetostrictive composite sensor which shows promise for the sensing of both currents and magnetic fields while also being highly electrically isolated. Potential applications for this sensor include sensing in HV current sensing (e.g. power transmission infrastructure, HV test facilities) and high magnetic field strength sensing (e.g. Magnetic Resonance Imaging).

1.2 Thesis Objective

The objective of this thesis is to document new insights into the theory, modeling, and testing of the optical sensors based on an FBG magnetostrictive composite, designed and developed at UWM, with the overarching goal to determine their immunity from thermal disturbances. There have been several studies, including those performed by Lopez et al., Lasassmeh, and Frailey [4]–[6] among others, demonstrating the use of magnetostrictive composites coupled with FBGs to accomplish the tasks of sensing both magnetic fields and currents.

Magnetic fields and by extension currents are measured by this sensor in terms of the optical power reflected from the device. This reflected power is proportional to the integration of the spectral reflectance of the FBG.

The sensor developed at UWM was done so under the assumption that uniform strain, when applied to an FBG, should yield little to no change in the spectral shape and width of the reflectance for the FBG embedded in the composite.

Since the reflected power of the sensor is proportional to the integration of the spectral reflectance, an even thermal distribution will result in a uniform strain on the FBG and thus no change in the output power is expected due to a change in the ambient temperature.

It is essential to understand the thermal characteristics for any current/magnetic field sensing device since such characteristics determine when and where sensors are appropriate to be used. If a sensor's accuracy degrades with temperature fluctuations, it can have a significant effect on the

usefulness of the sensor as a sensing device. For example, if a sensor were to have a 5% tolerance within a 20°C window, the sensor would most likely prove to be useful in most applications over that range, however; if the sensor had a 50% tolerance over the same range, the usefulness of the sensor over the range specified would be greatly diminish.

1.3 Thesis Structure

Chapter 2 will cover theory of various topics that are necessary to understand how the sensor works and the physics that impact the sensors response to environmental factors (e.g. magnetic fields, temperature, etc.).

Chapter 3 will go into detail of the computational methods that were employed in an effort to predict the magnetic and thermal response of the magnetostrictive composite sensors.

Chapter 4 will discuss the manufacturing of the magnetostrictive composite sensors.

Chapter 5 will go into detail the experimental methods employed during the course of the study along with details of changes made along the way.

Chapter 6 will discuss the observations made, limitations discovered, and conclusions drawn from the experimental results and simulations performed. This chapter also discusses the need for further investigation based on observations during the course of running experiments on the sensors.

Chapter 2

2 Theory

2.1 Mechanical Deformation

Deformation, in engineering, refers to the process of changing the size and/or shape of a material. There are two main categories of deformation: elastic deformation and plastic deformation. Plastic deformation is the deformation of a material in which the material does not return to its original shape and elastic deformation is when a material that is deformed, either through applied force or other means, returns to its original shape or size when that external factor is removed. For the understanding of this thesis, a more in-depth background on elastic deformation is warranted.

Hooke's law, discussed in Callister [7], is defined as

$$\sigma = E \epsilon \quad , \quad (1)$$

where σ is engineering stress, ϵ is engineering strain, and E is the elastic modulus, also known as Young's Modulus.

Engineering stress is synonymous with pressure in that the units are force per unit area. The equation defining engineering stress is given as

$$\sigma = \frac{F}{A_0} \quad , \quad (2)$$

where F is the force applied to the sample and A_0 is the initial cross sectional area of the sample.

Engineering strain is defined as

$$\epsilon = \frac{\Delta l}{l_0} , \quad (3)$$

where Δl is the change in length with respect to the original length of the sample, l_0 .

2.2 Magnetostriction

Magnetostriction, first identified in 1842 by Joule [8], is the property of a material to alter dimension when exposed to a magnetic field. This alteration in dimension is due primarily to magnetic domain and magnetic boundary effects stemming from magneto-crystalline anisotropy, a phenomenon experienced in ferromagnetism where more energy is required to magnetize a material in one direction than another, discussed in Abbundi et al. and James et al. [9], [10]. A simplified illustration of magnetostriction is shown in Figure 1.

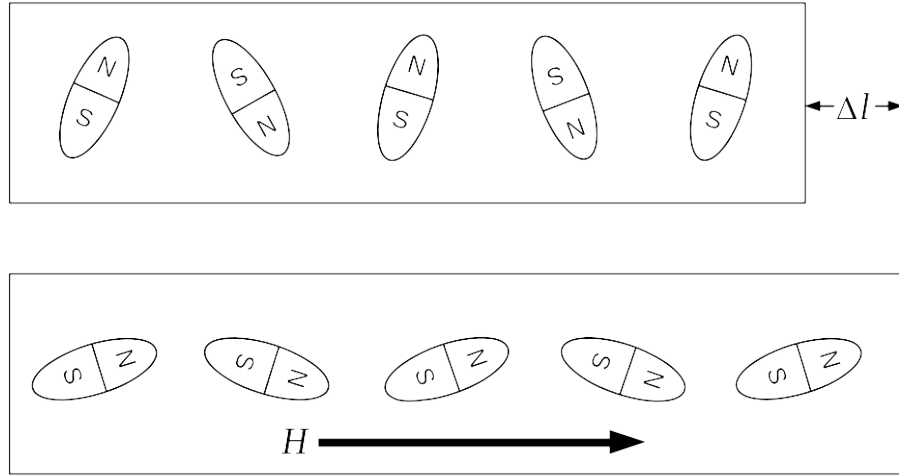


Figure 1: Magnetostriction, where H is applied magnetic field strength and Δl is the change in length of the material

Terfenol-D, a magnetostrictive alloy developed by the Naval Ordnance Laboratory, having the formula $Tb_xDy_{1-x}Fe_2$ with $x=0.3$, has the largest known magnetostriction at up to 2000 ppm strain, Abbundi et al. [9].

Cullity et al. and Kellogg et al. [11], [12], indicate that for a magnetostrictive material, magnetostriction can be defined in terms of the materials magnetization as:

$$\lambda = \frac{3}{2} \lambda_s \left(\frac{M^2}{M_s^2} \right), \quad (4)$$

where λ is the magnetostrictive strain, λ_s is the mechanical stress free saturation value of the magnetostrictive strain, M is the magnetization, and M_s is the saturation value of the magnetization.

Assuming a randomly distributed homogeneous distribution of particles in a magnetostrictive composite (e.g. epoxy particle matrix), equation 4 can be extended as

$$\lambda_{ii} = \frac{3}{2} \lambda_s \left(\frac{M_i^2}{M_s^2} \right) , \quad (5)$$

where the subscript index i is exclusively the Cartesian x,y, or z coordinate.

Given a randomly distributed homogeneous distribution of particles in a magnetostrictive composite, λ_s is assumed constant, thus a constant c_1 is defined as

$$c_1 = \frac{3}{2} \lambda_s , \quad (6)$$

and equation 5 becomes

$$\lambda_{ii} = c_1 \left(\frac{M_i^2}{M_s^2} \right) . \quad (7)$$

Given that M_s is also a constant for a randomly distributed homogeneous distribution of particles , a second constant c_2 can be defined as

$$c_2 = \frac{c_1}{M_s^2} , \quad (8)$$

and equation 7 becomes

$$\lambda_{ii} = c_2 M_i^2 . \quad (9)$$

Rearranging and solving equation 9 for M_i yields

$$M_i = \sqrt{\frac{\lambda_{ii}}{c_2}} . \quad (10)$$

Defining a third constant c_3 as

$$c_3 = \sqrt{\frac{1}{c_2}} , \quad (11)$$

equation 10 becomes

$$M_i = c_3 \sqrt{\lambda_{ii}} . \quad (12)$$

Equation can be rearranged as

$$\lambda_{ii} = \left(\frac{M_i}{c_3} \right)^2 . \quad (13)$$

The results in equations 12 and 13 prove useful for computational modeling of magnetostriction and allows the development of an B-H curve for simulation from existing strain versus magnetic field data in conjunction with magnetization versus magnetic field data.

Taking this idea further, substituting M_i in the expression for magnetic flux density

$$B_i = \mu_0 (H_i + M_i) , \quad (14)$$

where μ_0 is the permeability of free space, H_i is magnetic field strength, and M_i is the magnetization of the material.

Equation 14 becomes

$$B_i = \mu_0 (H_i + c_3 \sqrt{\lambda_{ii}}) . \quad (15)$$

Equation 15 describes the magnetic flux density within the magnetostrictive composite material along coordinate i , assuming a homogeneous, randomly oriented particle composite. If this is not the case, c_3 would be different for the x, y, and z coordinate.

2.3 Fiber Bragg Grating

An FBG is an optical device, built into a small section of optical fiber with periodic modulation of the refractive index, that reflects light at a certain wavelength (known as Bragg wavelength) while allowing the remaining light to pass through. The two main parameters that effect the reflectance and transmittance of an FBG are the grating period Λ (periodicity of the index modulation), and grating index of refraction n , shown in Figure 2.

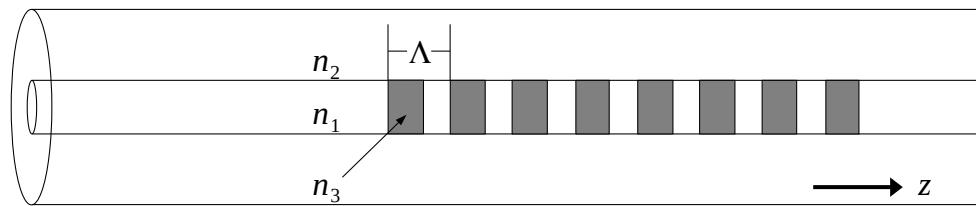


Figure 2: Fiber Bragg grating with uniform grating Λ , where n_1 , n_2 , and n_3 correspond to the core, cladding, and FBG grating refractive indices

There are many ways in which a grating can be formed and distributed within an optical fiber core including uniform grating, chirped grating, and apodized grating. In a uniform grating, the gratings in the FBG are distributed evenly with the same period of modulation index as shown in Figure 2. Chirped gratings are composed of gratings that are non-uniformly distributed, varying in grating period and also in grating width as shown in Figure 3.

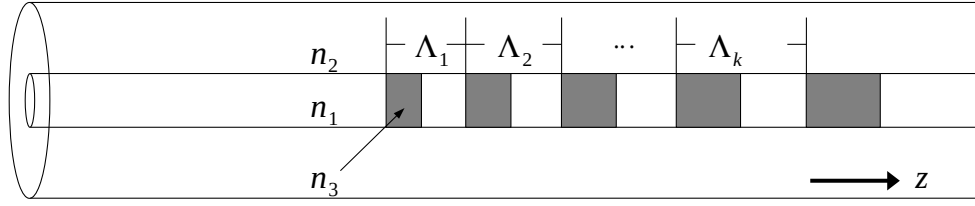


Figure 3: Chirped fiber Bragg grating with non-uniform grating period

Apodization is accomplished by varying the refractive index along the length of the FBG as shown in Figure 4.

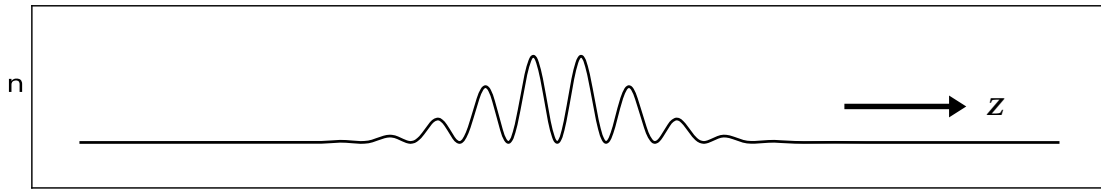


Figure 4: Fiber Bragg grating Gaussian apodization

FBGs can be mathematically modeled with the transfer matrix method as discussed in detail in Prabhugoud et al., Lasassmeh, Frailey, and Mueller [5], [6], [13], [14]. The key take away from these sources are the transfer functions described in equation 16

$$\begin{bmatrix} R_k \\ S_k \end{bmatrix} = F_k \begin{bmatrix} R_{k-1} \\ S_{k-1} \end{bmatrix}, \quad (16)$$

where R is the amplitude of the forward propagating mode, S is the amplitude of the backward propagating mode, k is FBG section number and

$$F_k = \begin{bmatrix} \cosh(\gamma_B \Delta z) - j \frac{\hat{\sigma}}{\gamma_B} \sinh(\gamma_B \Delta z) & -j \frac{\hat{\sigma}}{\gamma_B} \sinh(\gamma_B \Delta z) \\ j \frac{\hat{\sigma}}{\gamma_B} \sinh(\gamma_B \Delta z) & \cosh(\gamma_B \Delta z) + j \frac{\hat{\sigma}}{\gamma_B} \sinh(\gamma_B \Delta z) \end{bmatrix}, \quad (17)$$

with j being the unit imaginary number. Equation 17 shows that F_k is a function of the length of the FBG section Δz with parameters γ_B (a function of DC and AC coupling coefficients) and the DC coupling coefficient $\hat{\sigma}$.

2.4 Thermal Expansion

Thermal expansion is a material dependent property where dimension changes in response to a change in its internal temperature. There are three main classes of thermal expansion: linear, area, and volume. Thermal expansion in uniform solids can be modeled using a linear expansion model. This model takes on the form

$$\epsilon_T = \alpha_L \Delta T, \quad (18)$$

where ϵ_T is thermal strain, α_L is the linear coefficient of thermal expansion (LCTE), and ΔT is the change in temperature, Tummala et al. [15].

It has been shown in Duenas et al. and Tummala et al. [15], [16], that for a homogeneous epoxy composite matrix, that the thermal strain follows equation 18 and that the LCTE α_L is a function of the volume ratio of epoxy to filler material.

2.5 Moisture Expansion

Moisture related expansion of molding compounds including epoxy composites is described in Teverovsky [17]. It is a material dependent property where dimension changes in response to a

change in the materials internal moisture content. According to Teverovsky, the relationship between strain and moisture swelling in the molding compound is given by

$$\epsilon_{sw} = CME \cdot \delta_{MC}^m \quad , \quad (19)$$

where ϵ_{sw} is moisture swelling induced strain, CME is the coefficient of moisture expansion, and δ_{MC}^m is the moisture uptake of the molding compound.

2.6 SLED

A superluminescent light emitting diode (SLED), described in Lee et al. and Alphonse et al. [18], [19], are a type of light emitting diode that exhibits a high optical power and large bandwidth. An Exalos EXS1520-2111 1550 nm SLED was used for experiments performed. Specific properties for the SLED are shown in Table 1.

Max Power	16.48 mW
Peak Wavelength	1549.9 nm
Central Wavelength	1547.1 nm
Bandwidth	63.1 nm

Table 1: SLED parameters @ T=20°C, I=500mA

2.7 Heat Transfer

There are three main mechanisms of heat transfer: conduction, convection, and radiation as laid out in Levenspiel [20]. For the purpose of the thesis, conduction (the transfer of heat between objects in contact) and convection (transfer of heat with environment through fluid motion) are the primary means of heat transfer in the experiments carried out for this thesis.

Thermal equilibrium, is the concept that two bodies are in a state where no thermal energy flows between them, as described in the NASA publication “Thermodynamic Equilibrium” [21]. For the sake of this thesis, it is inferred that a specimen is at thermal equilibrium when it approaches a state of negligible change in temperature over a given period of time.

Chapter 3

3 Computational Modeling

The overall goal of the computation modeling effort was to create a unified model of the sensor that is capable of modeling both the magnetostrictive effect and thermal expansion effect on the sensor. The sections in this chapter will cover the tools used and work performed toward this goal. Ultimately, a working unified model has not been achieved; however, the methods developed have made progress toward the creation of a unified model and have shed light on additional information needed to create a fully functional unified model.

3.1 Octave Modeling

Octave scripting is used to approximate the optical spectrum reflected from the sensor as a function of an input mechanical strain profile generated using Comsol. The scripting is broken into two main parts:

- Comsol strain data pre-processing
- FBG reflected spectrum computation

The Comsol strain data pre-processing script performs the following:

- Truncates data to the size of the FBG
- Uses a polynomial fit to generate evenly spaced data points

- Computes first derivative of interpolated strain profile

The FBG spectral reflectance computation script, based on Prabhugoud et al. [13] and work previously done by Mueller [14], was modified to accept the interpolated strain profile and derivative of the interpolated strain profile from the Comsol strain data pre-processing script.

The two scripts compute the spectral reflectance and spectral power density based on the input strain profile generated with Comsol.

The optical spectrum is integrated to obtain total reflected power and is subsequently normalized.

3.2 Comsol Modeling

3.2.1 Composite Curing

Two main effects were modeled based on sensor magnetostrictive composite curing parameter: 1) FBG prestress and 2) epoxy shrinkage. Initial stress was added to the model for the FBG based on the data provided in Frailey [6], which states that a total mass of 30 grams was suspended from the FBG during the sensor curing process. Given that the FBG core plus cladding is 125 μm , a resulting prestress of ~24MPa is applied to the FBG during curing of the sensor; however, an initial stress of three times this value was used for the results presented in section 3.2.3, producing results closer to those experimentally observed. Initial strain was added to the composite material within the Comsol model in order to model the shrinking effect, discussed in Khoun et al. [22], of the epoxy during the composite curing process. The initial strain of the composite material was adjusted until the spectrum resulting from the Comsol model strain, post-

processed in Octave, had a peak wavelength approximately matching with that of the spectrum taken for the trapezoidal slab sensor at 20°C in the water bath experiments discussed in the section 5.

There are still factors during the curing process that affect the overall accuracy of the simulated reflected spectral shape and thus the simulated reflected optical power of the sensor that are not accounted for in the model. One factor that has not been properly accounted for is the effect of curing the sensor in the presence of a magnetic field. So far what has yielded the closest results is applying a linear initial strain gradient, along the axis of the composite material running parallel to the embedded FBG, in conjunction with the offset to compensate for shrinkage during the epoxy curing process. Another factor is the effect of relative humidity in relation to the CME of the composite material during and after the curing process.

3.2.2 Magnetostriction

In order to model magnetostriction in Comsol, a B-H curve was developed using magnetostriction equations discussed in section 2.2. The B-H curve was created in LibreOffice Calc using a combination of the M-H curve found in Lo et al. [23] in the figure labeled “Fig. 3”, the 27% λ -H curve found in Liu et al. [24] in the figure labeled “FIG. 3”, and a combination of equations 12 and 14. To create the B-H curve for Comsol, the following steps were taken:

1. Data from [23] and [24] was extracted using the WebPlotDigitizer developed by Rohatgi [25].

2. Magnetization M_i was calculated using equation 12 with the extracted λ -H curve data.
3. Magnetic flux density B_i was calculated using a combination of H_i from the λ -H curve data and M_i calculated in the previous step.
4. The built-in solver was used to find the value of c_3 such that M_i equaled the value for the maximum H_i value in the extracted M-H curve.

The resulting B-H curve is shown in Figure 5.

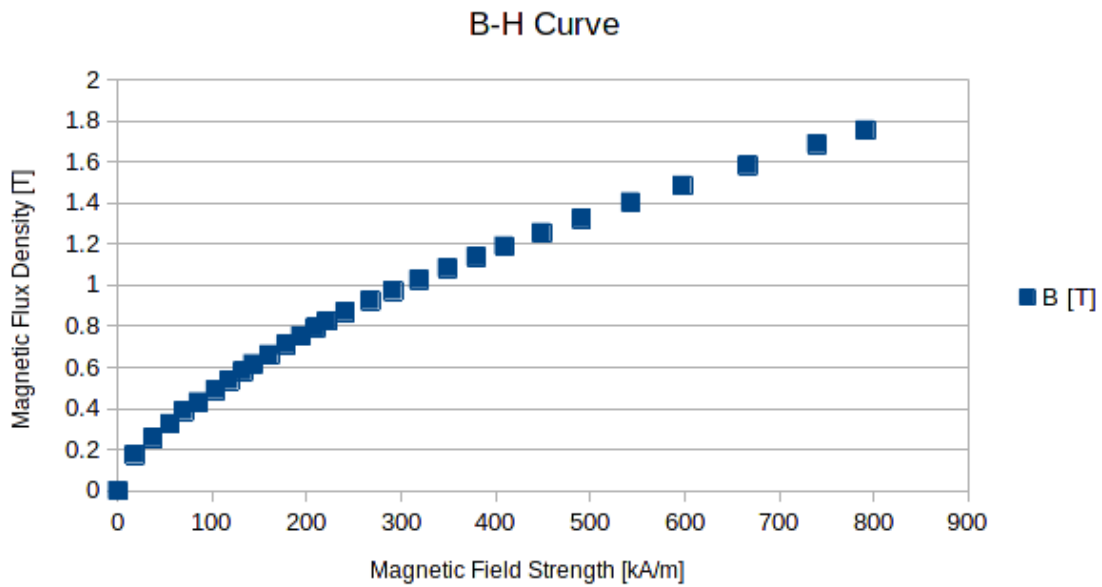


Figure 5: Comsol model B-H curve 27% composite volume fraction

Using equation 13 within the Comsol model, without composite curing effects, and running the strain data generated through the Octave scripts to approximate the FBG response yields the results shown in Figure 6, which are consistent with results shown in Frailey [6] “Figure 4-13”.

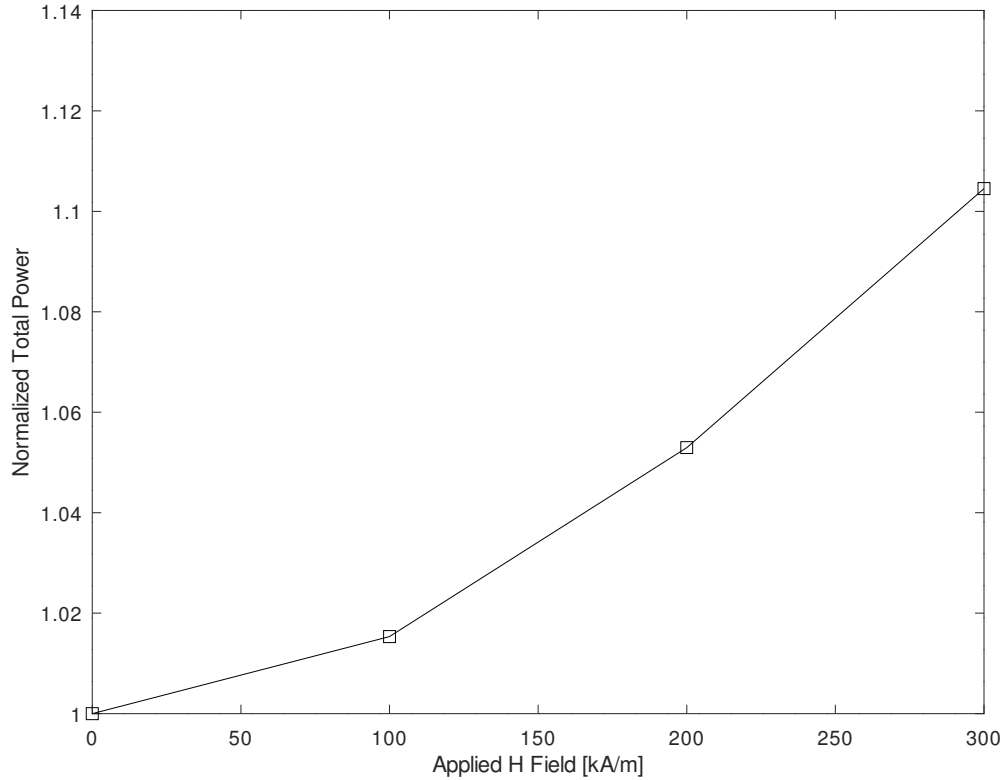


Figure 6: Simulated trapezoidal sensor FBG optical response computed from resulting strain found in Comsol using new B-H curve and post processed using Octave scripting

3.2.3 Thermal Expansion

LCCTE for the model was iteratively tuned such that the peak of the spectrum output by the Octave scripts described in section 3.1, matched the empirical data obtained for the trapezoidal slab sensor obtained during the water bath experiments, discussed in section 5. Using this method, the LCCTE for the sensor magnetostrictive composite material was estimated to be approximately 76 ppm/°C. An example of the simulated spectrum generated for the trapezoidal slab sensor is shown in Figure 7.

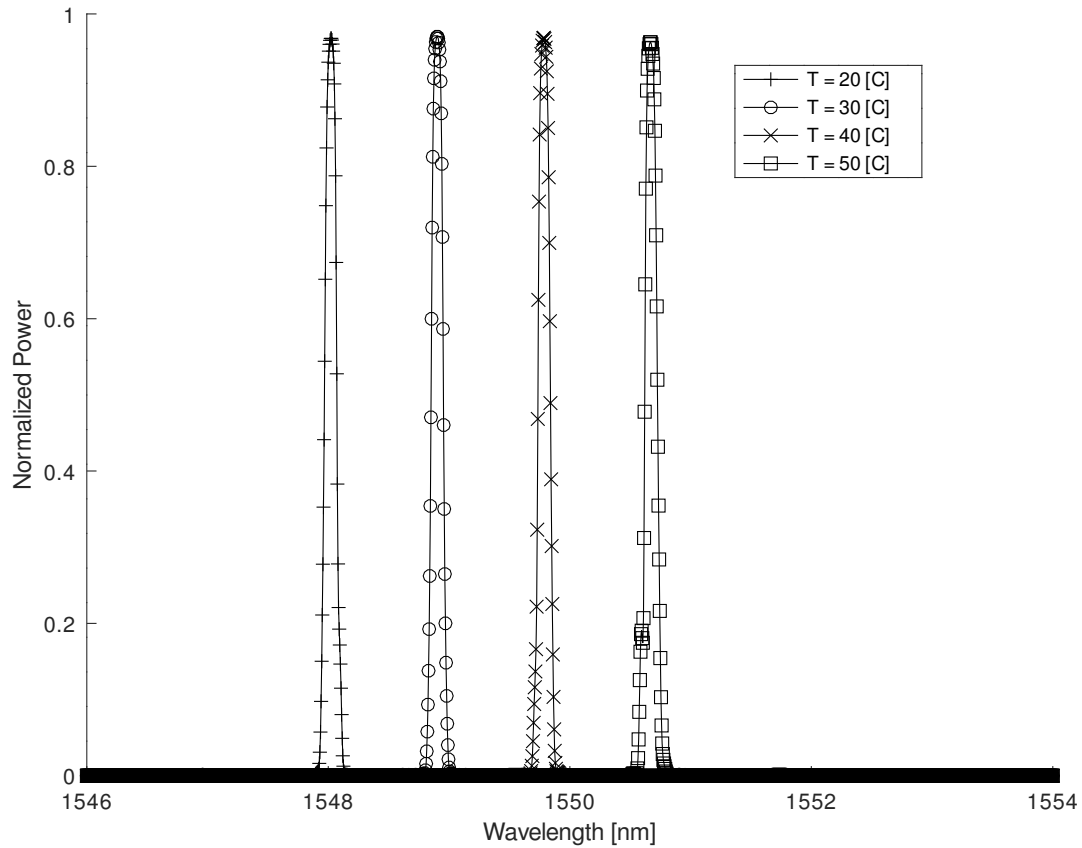


Figure 7: Simulated normalized trapezoidal slab reflected spectral power after adjusting LCTE in Comsol model

A parametric sweep of temperatures were performed in an effort to gauge the models ability to predict the sensor reflected optical power as a function of temperature. Due to the sensitive nature of FBGs and a lack of understanding of the effects of curing the composite material in the presence of a magnetic field, as discussed in section 4, along with potential effects of moisture on the cure process, the accuracy of the model in predicting the thermal effect of the change in sensor reflected optical power are questionable at best and future work is needed to better hone in the model to account for these effects. An example of the simulated normalized reflected optical power of the sensor is shown in Figure 8.

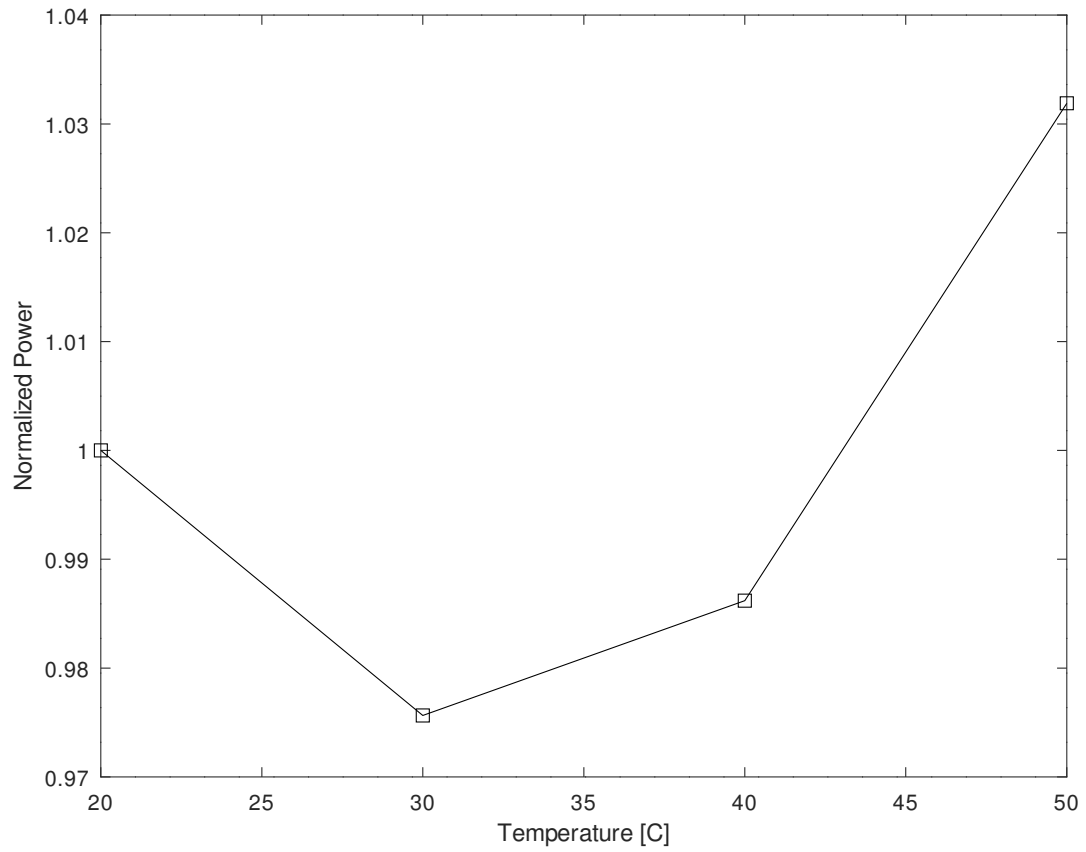


Figure 8: Trapezoidal slab normalized simulated reflected power

Chapter 4

4 Sensor Manufacturing

There have been many magnetostrictive sensor designs developed both at UWM and at other institutions. Quite a few designs do not attempt to address the issue of thermal expansion in the proposed designs. For instance, some designs do not consider the compensation for thermal expansion and infer magnetic fields by measuring the Bragg wavelength shift observed in the FBG reflectance. Given that both thermal expansion and magnetic field induce a shift in the Bragg wavelength of the FBG, thermal expansion compensation is not feasible without additional input.

Several years ago the idea of using various shapes of Terfenol-D/epoxy composite material, bonded with various shapes of plain cured epoxy resin, was investigated in an effort to create chirping (non-uniform strain distribution) on embedded FBGs in order to evoke a change in optical power reflected from the sensor. During the course of these investigations, it became apparent that the shape of the magnetostrictive composite, without additional components, could be used to tune the magnetic flux distribution within the magnetostrictive composite and elicit the desired chirping effect on the FBG when exposed to an external magnetic field.

The first such sensor relying on this magnetic flux distribution shaping to be modeled, manufactured, and tested was a conical sensor discussed in Lasassmeh, Frailey, and Jimenez-Mejia et al. [5], [6], [26]. Comsol modeling for this conical shaped sensor indicated that this

sensor should exhibit little to no change in the reflected optical power as a function of change in ambient temperature. This sensor was initially manufactured with a two stage embedding method where the magnetostrictive composite was molded into its final shape using a silicon mold with a piece of music wire (e.g. guitar string) embedded into the sensor. The music wire was then removed by pulling the music wire out of the sensor post-cure and embedding an FBG using a low viscosity epoxy in conjunction with capillary action to draw the low viscosity epoxy into the void between the magnetostrictive composite and the FBG. This method often resulted in poor bonding between the composite material and the optical fiber.

A second, more challenging, method was developed in an effort to achieve better bonding where the FBG was embedded into the magnetostrictive composite at the same time as the composite material cured in the silicon mold. This new FBG embedding method proved troublesome to manufacture since the curing of the conical shape tended to induce a strain gradient on the FBG during the curing process.

The approach of molding the magnetostrictive composite into the final shape was abandoned by Frailey [6] in favor of molding rectangular prism magnetostrictive composite slabs with the FBG embedded during the curing of the composite material. This change in manufacturing has shown the least augmentation of the shape of the reflected FBG spectrum following the composite curing process. After curing the slab is modified into the final desired shape using a table mount wet sanding tool.

The two shapes investigated for thermal response are the trapezoidal slab and the acute Saccheri quadrilateral. The samples tested were manufactured by and discussed in Frailey [6] having dimensions shown in Tables 2 and 3 corresponding to Figures 9 and 10 respectively.

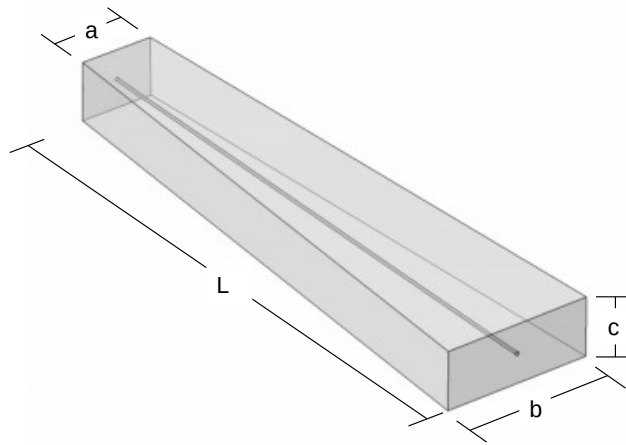


Figure 9: Trapezoidal slab

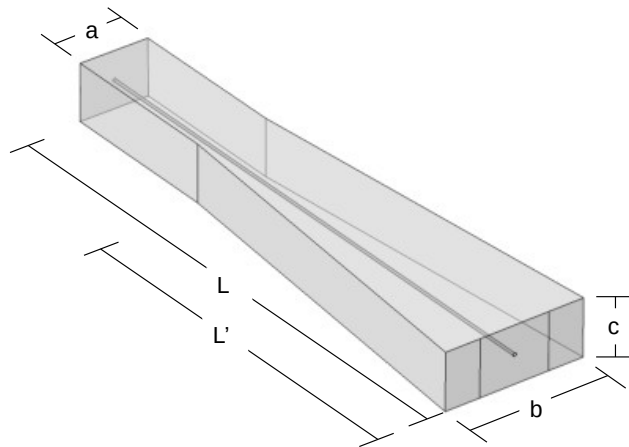


Figure 10: Acute Saccharin quadrilateral slab

Dimension	Size [mm]
a	5.3
b	10.2
c	3.2
L	40

Table 2: Trapezoidal slab dimensions

Dimension	Size [mm]
a	5.3
b	10.2
c	3.2
L'	28
L	40

Table 3: Acute Saccharin quadrilateral slab dimensions

Each sample was manufactured with a volume fraction of 30% Terfenol-D:epoxy, and having 30g weight suspended from the FBG, adding in 5g increments in 5 minute intervals, while also immersing the sensor in an external magnetic field during the curing process, in a similar manner as shown in Figure 11.

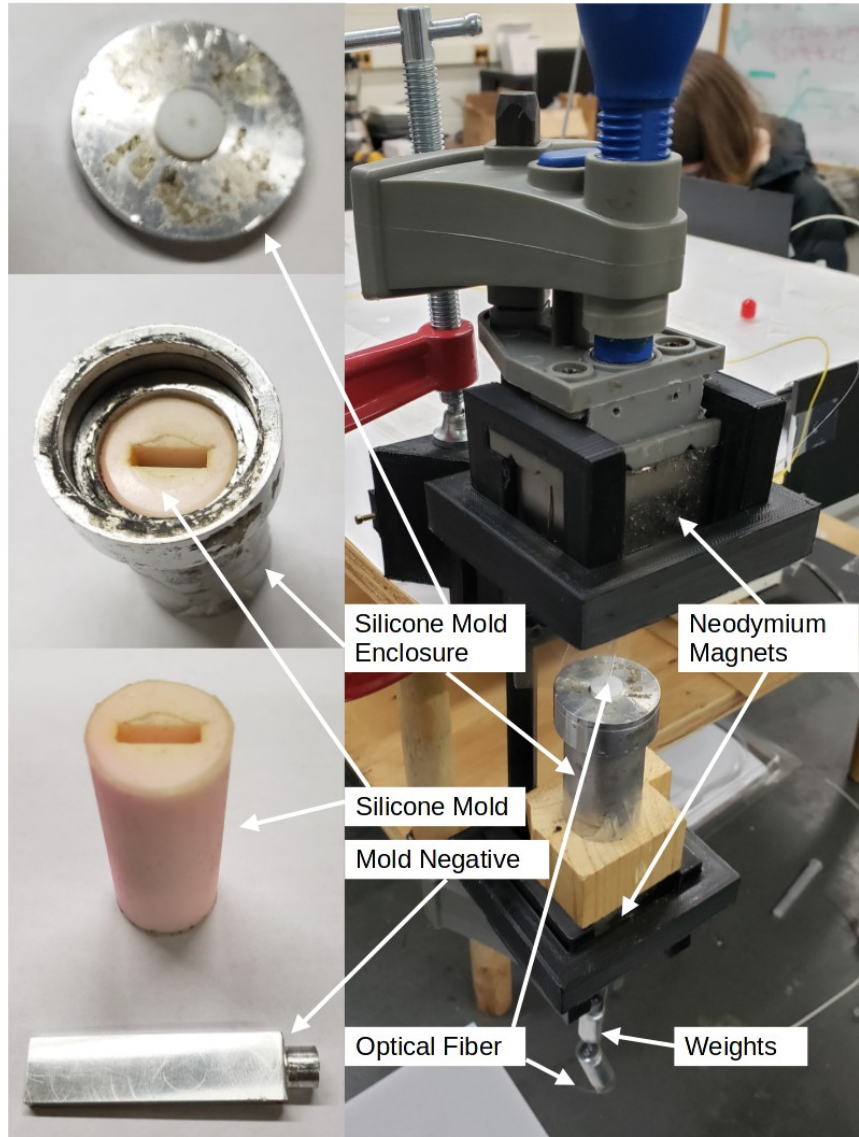


Figure 11: Magnetostrictive composite slab molding setup

Chapter 5

5 Experimental Methods

Initially, the research plan was to test the two prototype sensors, (trapezoidal slab and acute Saccharin quadrilateral slab) described in section 4, in-person, in the thermal chamber described in this chapter. Due to current events and safety concerns, that testing was put on hold after only one experiment was conducted and a new plan was developed to include a water bath setup to allow the experiments to be conducted remotely in a safe manner. Sections 5.2 and 5.3 that follow cover the hardware/electrical design, optical circuit design, experiment design, data analysis, and results obtained for both the thermal chamber and water bath experiments.

5.1 Optical Design

The optical circuits for the thermal chamber experiments, shown in Figure 17, consists of an SLED, optical coupler, photodetector, optical circulator, prototype magnetostrictive sensor, and optical spectrum analyzer. The SLED serves as the optical source for the experiments, with its output being directed via optical fiber to an optical coupler. The optical coupler splits the incident light on the device and redirects a percentage of the input light out one of two output ports. The first output of the optical coupler is directed towards a photodetector while the second output port is directed to the optical circulator, a device which takes light in one port and redirects it to the next port on the device. The light from the second output of the optical coupler enters the first port of the optical circulator and then exits the second port of the optical circulator which is connected to the sensor being tested. Light at the Bragg wavelength of the FBG embedded in the

sensor is reflected back and enters port two of the optical circulator and is subsequently redirected out of port three of the optical circulator. After being redirected out of port three of the optical circulator, the light enters the input port of the optical spectrum analyzer.

The optical design for the thermal chamber experiment performed was altered from that used in Frailey [6] for the measurement of sensor response to applied magnetic field. The modifications were made in order to gather data required to compensate for the thermal drift of the SLED source used in the experiments. The primary differences between the setup used for the thermal experiment described in section 5.2 and those performed in Frailey [6] is that the optical coupler, which was located after the optical circulator in the magnetostrictive response experiments, is now located before the optical circulator. The change allows a percentage of the light from the SLED source to be sent directly to a photodetector circuit, allowing for the indirect determination of relative change in the optical power of the SLED source for the duration of the thermal experiments. The only drawback of moving the optical coupler in the optical circuit is that the optical power incident on the FBG within the sensor is reduced based on the percentage of power that is sent by the optical coupler to the photodetector.

Later, during the initial water bath experiments described in section 5.3, it was realized that a more accurate optical coupling coefficient (the ratio of SLED source light incident on the photodetector and on the sensor) could be more accurately determined if the source was modulated upstream of the optical coupler. An electronically controlled optical attenuator was added to the experimental setup, as shown in Figure 12, during the course of the water bath thermal experiments in order to periodically modulate the power of the SLED as it enters the

optical path. This modulation allows for the proper alignment of experimental data and a more precise determination of the optical coupling factor for the two branches of the optical circuit that are located after the optical coupler.

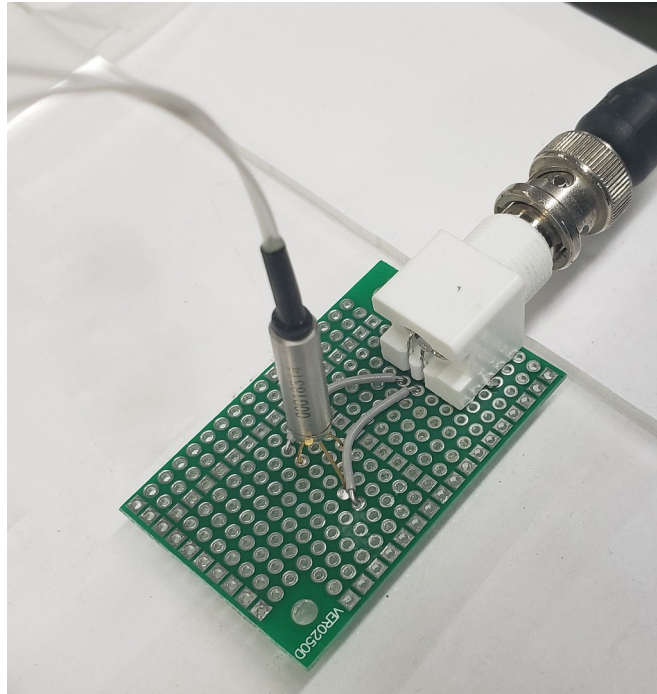


Figure 12: Computer controlled optical attenuator

5.2 Thermal Chamber

Only one experiment, performed on the trapezoidal sensor, was conducted using the thermal chamber described in the following sections due to lab shutdowns and safety restrictions due to current events. The thermal chamber design, experiments, data analysis, and results are described in the following sections.

5.2.1 Thermal Chamber Design

To test the thermal properties of the sensor, a custom thermal chamber and control system were developed to accurately control the experiment temperature and ensure a uniform temperature distribution throughout the thermal chamber. The completed thermal chamber is shown in Figure 13.

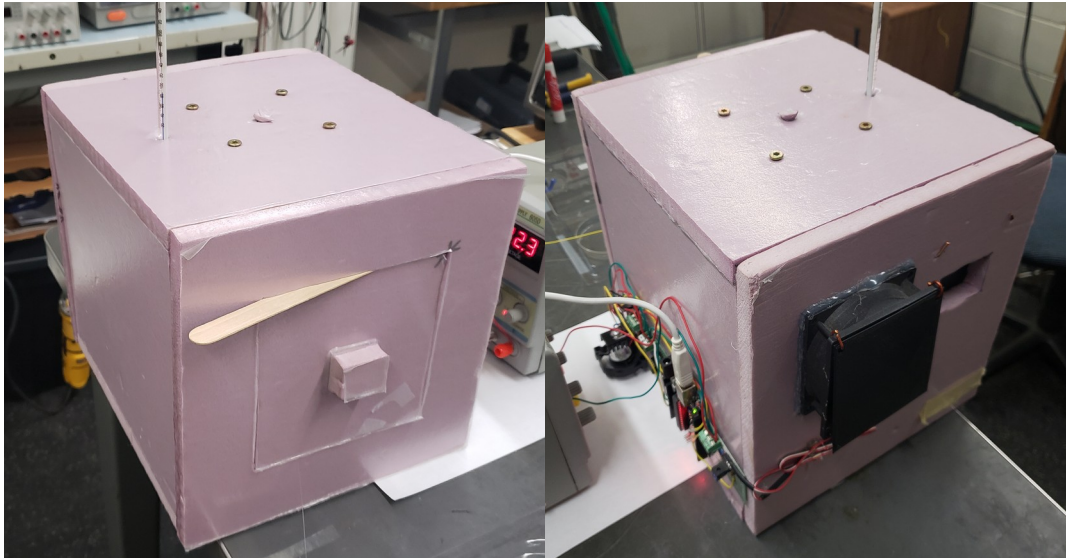


Figure 13: Thermal chamber front view (left) and rear view (right)

The thermal chamber exterior is constructed using rigid foam board insulation, cut to size using a combination of hot wire and utility knife and joined together using hot melt adhesive (HMA).

A circulator fan, shown in Figure 14, is mounted at the top of the thermal chamber and runs continuously to ensure air inside the thermal chamber is thoroughly mixed and maintains a homogeneous temperature throughout.

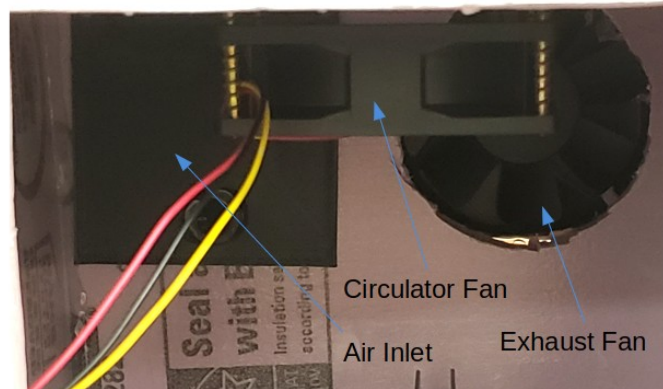


Figure 14: Thermal chamber (inside view) air flow components

The heat source for the thermal chamber, shown in Figure 15, consists of two automotive light bulbs, wired in parallel, and affixed to an aluminum plate using a two part epoxy adhesive. The heating element is capable of dissipating 45W at an input voltage of 12V.

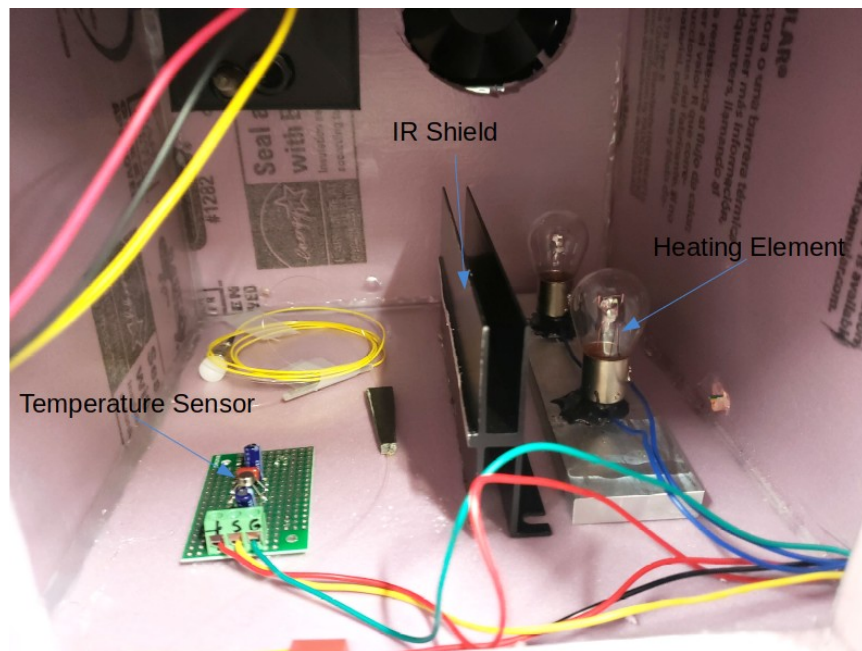


Figure 15: Thermal chamber (inside view) heating element, IR shield, and temperature sensor

The thermal chamber is partitioned into two parts: 1) Heating element area and 2) thermal experiment area. The heating element area is partitioned from the thermal experiment area by a piece of aluminum that is painted black. The purpose of the separator is to shield the infra-red radiation (IR) generated by the heating elements from interfering with the experiment.

At the rear of the thermal chamber is an inlet and outlet with a fan attached to the outlet to provide active cooling when necessary (e.g. when the set point of the controller is less than the temperature inside)

A LM35A precision centigrade temperature sensor, shown in Figure 15, having 0.5°C accuracy, is attached to the bottom of thermal chamber in the thermal experiment area with HMA.

The thermal chamber controller electrical scheme is shown in figure 16 and consists of the following components:

- Arduino microcontroller
- Temperature sensor and low pass (LP) filter circuit
- Heating stage: metal-oxide-semiconductor field-effect transistor (MOSFET) based buck converter w/ custom made 45W heating element
- Cooling stage: MOSFET buck converter w/ exhaust fan
- Continuous duty air circulation fan

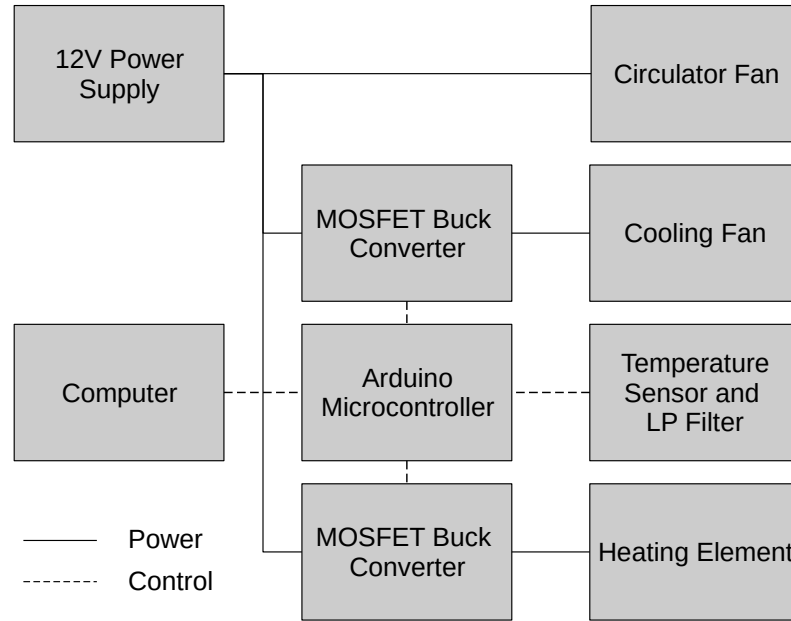


Figure 16: Thermal chamber electrical block diagram

The thermal chamber controller is divided into two parts: 1) Arduino firmware and 2) computer control and data acquisition interface. The Arduino firmware consists of a basic proportional integral (PI) controller, running in a 100ms hardware interrupt with fixed (hard coded in the firmware) proportional and integral gains. The temperature set point for the thermal chamber is adjustable via serial interface and the controller also provides feedback for external control via serial interface. See Figures 16 and 17 for more details. The computer control and acquisition portion consists of an experiment controller, written in MATLAB script, which controls the set point of the thermal chamber while also recording feedback from the thermal chamber regarding set point and temperature feedback, while also recording the voltage across the load resistor of a photodetector which monitors the output power of the SLED (EXS1520-2111), the light source for scanning the spectral response of an FBG.

While the experiment controller controls and monitors the thermal chamber via serial interface and gathers SLED power data via National Instruments (NI) data acquisition (DAQ) interface, a Thorlabs optical spectrum analyzer (OSA) is used to continuously gather optical spectral power density data for light reflected back from the FBG embedded in the sensor.

5.2.2 Thermal Chamber Experiments

The thermal chamber experimental setup block diagram is shown in Figure 17.

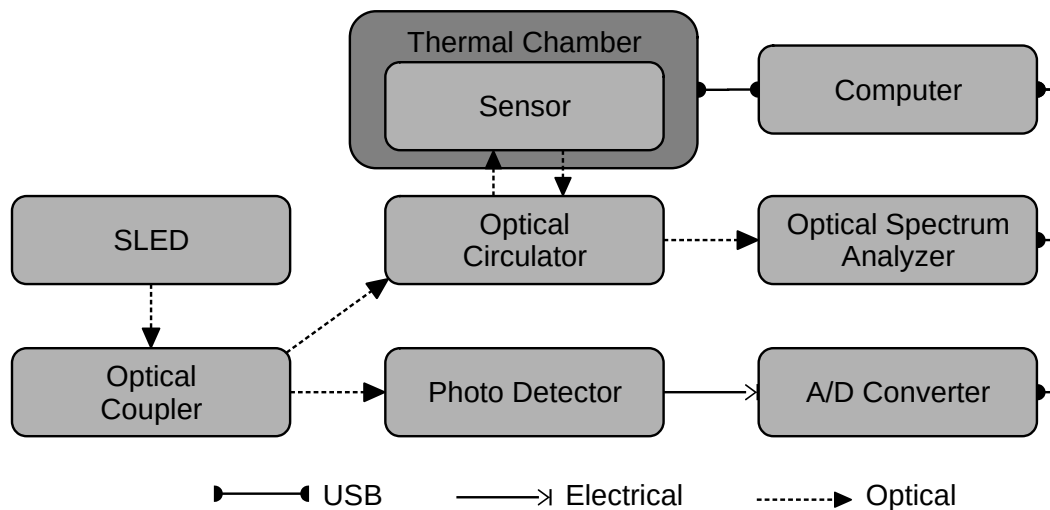


Figure 17: Thermal chamber experimental setup

The thermal chamber described in section 5.2.1 was used to gather experimental data to track the affect of temperature on the optical power reflected back from the FBG within the trapezoidal sensor for one experiment before being replaced with the water bath experiments. For this experiment, the trapezoidal sensor tested was placed approximately in the center of the bottom interior surface of the thermal chamber near the thermal chamber temperature sensor. The

thermal experiment consisted of four temperature set points: 20°C, 30°C, 40°C, and 50°C, and all set points were held for 1 hour.

For the 20°C set point, power to the heating and cooling buck converter stages were removed leaving the sensor at room temperature, which fluctuated in the range of 20°C to 20.5°C for the duration of this portion of the experiment. This was done to prevent the controller from turning the cooling fan on since the room temperature was slightly warmer than the set point and would have made the temperature less stable within the thermal chamber.

Data for the thermal chamber and SLED power were acquired in approximately 1 second intervals with small variations being introduced due to serial protocols and NI DAQ acquisition times. Spectra were acquired and recorded at a rate of approximately 1 sample per second (hardware limited) for the duration of the experiment.

5.2.3 Thermal Chamber Data Analysis

Data analysis and post-processing was performed using Python scripting. For this analysis, the desired outcome was to obtain the normalized reflected optical power of the trapezoidal sensor tested with respect to change in temperature in order to create a baseline measurement for subsequent water bath experiments that replaced the thermal chamber test method.

There are several parts to the thermal chamber experimental method data analysis including:

- Computing optical power reflected from sensor

- Interpolating SLED photodetector voltage (directly proportional to optical power) and sensor reflected power data for fixed time step
- Normalization of interpolated SLED photodetector voltage and interpolated sensor reflected power data
- Dividing normalized interpolated sensor reflected optical power by normalized interpolated input power to remove SLED source variation effects
- Taking a 60 second moving average window (LP filter)

The optical power for every spectra of the sensor was computed using trapezoidal numeric integration with the time vector computed based on the time embedded in the spectra file name in relation to the time embedded in the thermal chamber controller data file, stored in comma separated value (CSV) file format.

The analysis was complicated due to the thermal chamber and SLED power measurements being asynchronous in relation to the FBG spectra measurements obtained by the Thorlabs OSA. The analysis was further complicated due to the measurements not being taken at an exact fixed interval (e.g. measurements had dither). To overcome these analytic challenges, cubic interpolation was used to get both the SLED photodetector voltage and the sensor reflected power data into a fixed time step format. Results of the normalization of the SLED photodetector voltage and sensor reflected optical power are shown in Figure 18 and Figure 19 respectively.

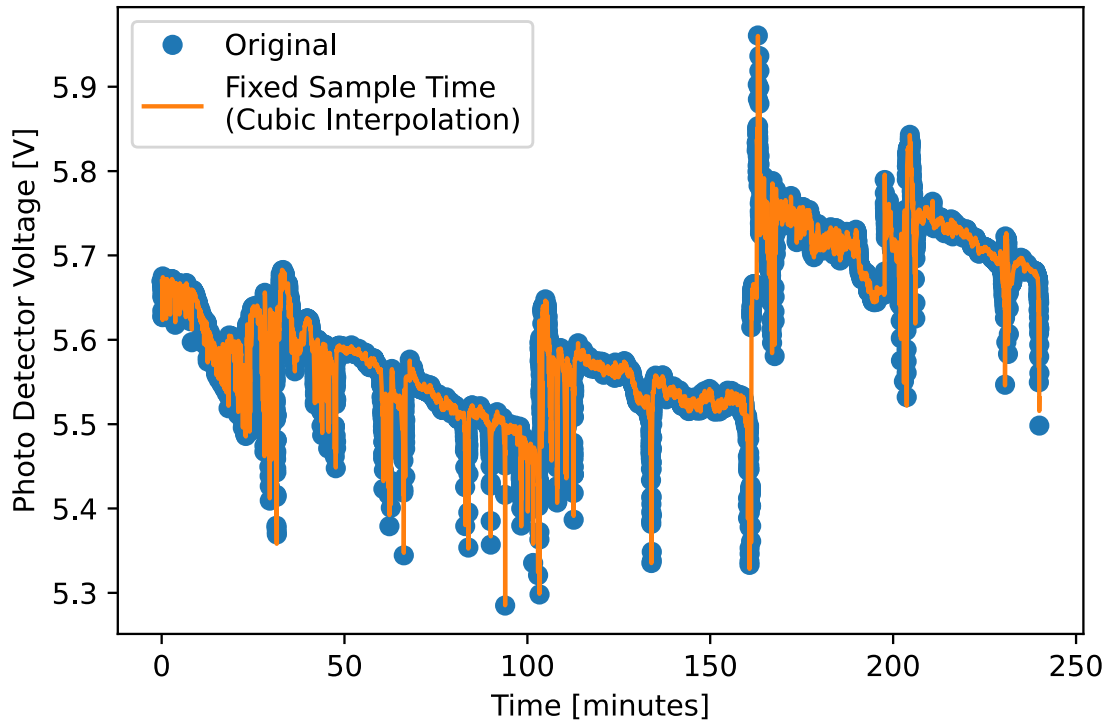


Figure 18: Thermal chamber experimental results - SLED output power measured in terms of photodetector voltage with a 3.8k load resistor

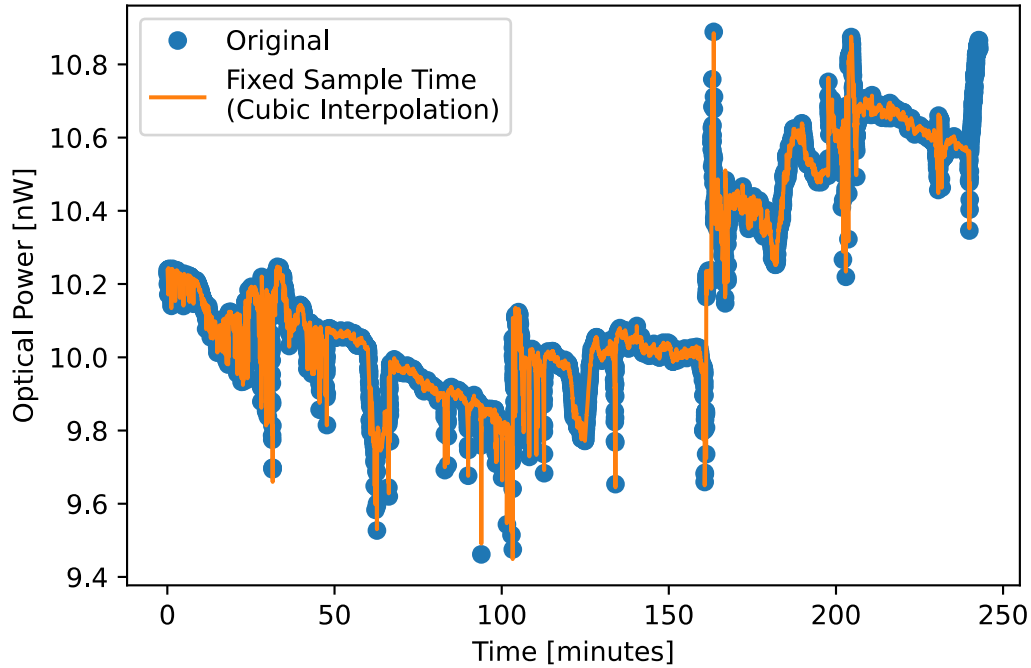


Figure 19: Thermal chamber experimental results - trapezoidal slab sensor reflected optical power based on integration of OSA spectrum

Following the interpolation of the data, both the SLED photodetector voltage and sensor reflected optical power are normalized with respect to the first point in the interpolated data sets. It should be noted that the SLED photodetector voltage is directly proportional to the optical power output by the SLED in the optical circuit. The normalized interpolated SLED photodetector voltage and normalized interpolated sensor reflected optical power are shown in Figure 20.

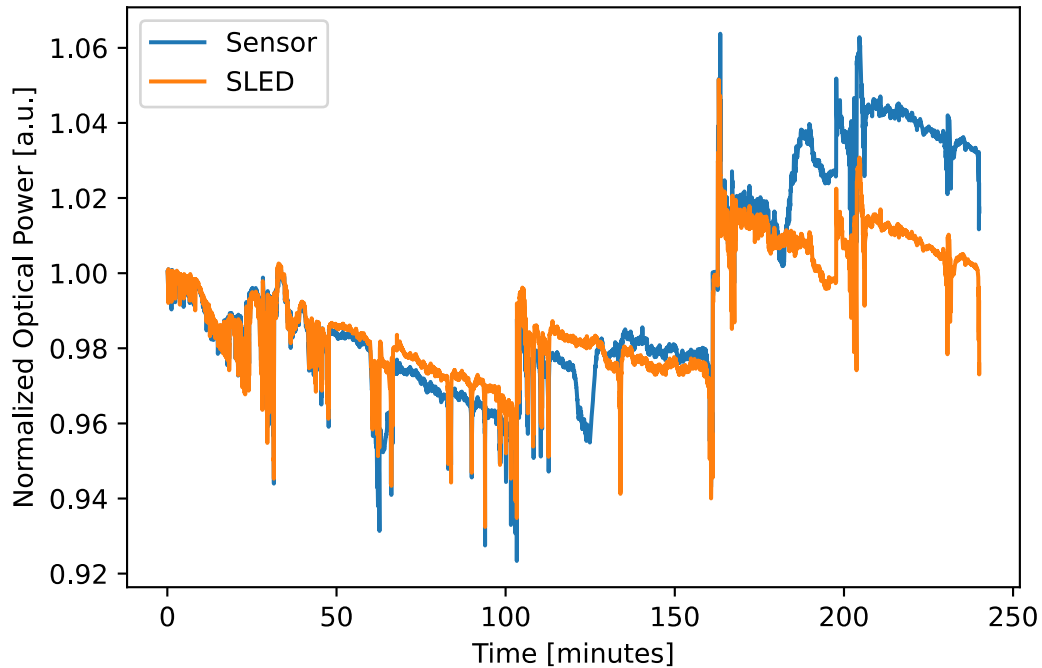


Figure 20: Thermal chamber experimental results - normalized sensor and SLED optical power for data in Figures 18 and 19

The normalization of the two data sets simplifies the removal of the effects of source power variations of the SLED input to the optical circuit. The removal of source variation is accomplished by dividing the normalized interpolated sensor reflected optical power by the normalized interpolated SLED photodetector voltage. For the thermal chamber data analysis, the optical coupling factor was assumed to be 1:1 based on the optical coupler specification. It was determined later that this value is affected by optical path variations after the optical coupler in the optical circuit and can introduce experimental error in the several percent range. Steps were taken to more accurately determine the optical coupling factor and mitigate this in the data analysis performed for the water bath experiments.

After the source variations were removed from the normalized interpolated sensor reflected optical power, a 60 second moving average of the data set was computed to smooth out artifacts left over from the division used to remove the SLED source variation for the results. The results of the removal of the SLED source variations and 60 second moving average are shown in Figure 21.

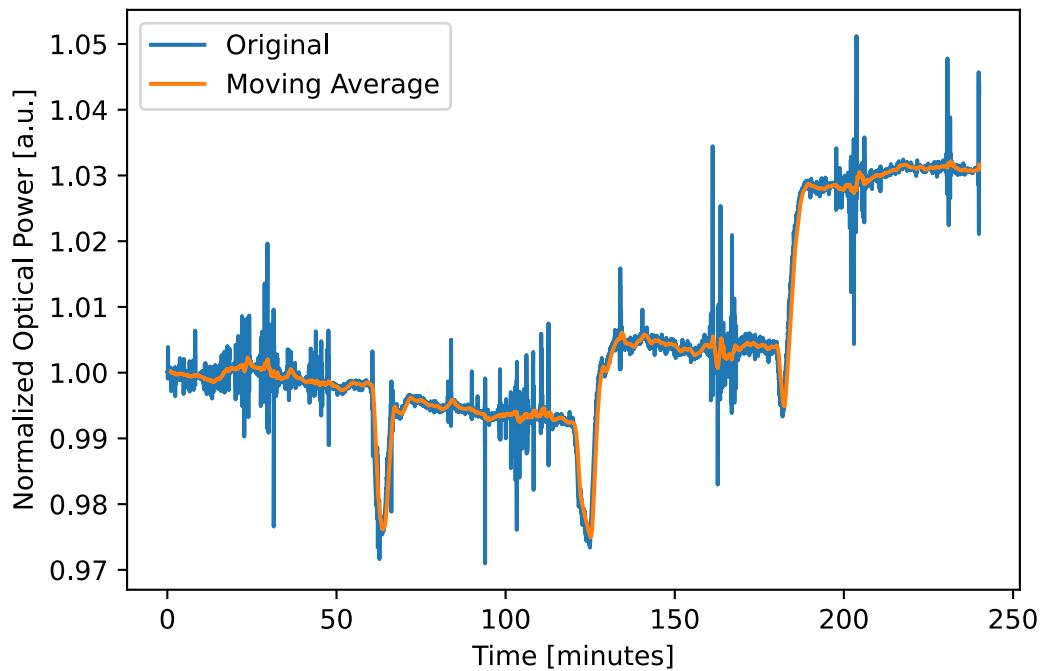


Figure 21: Thermal chamber experimental results - normalized sensor returned optical power for trapezoidal slab sensor in Figure 18 adjusted for SLED fluctuations with temperature in Figure 19

After the removal of the source variation from the normalized interpolated sensor reflected optical power data, 4th order polynomial fit coefficients for the normalized interpolated sensor reflected optical power vs temperature were computed. The polynomial fit coefficients were then used to determine the expected normalized sensor reflected power as a function of temperature

and subsequently re-normalized to the 20°C point. The final results of this analysis process are shown in Figure 22. These preliminary results, later superseded by the water bath experimental results discussed in section 5.3.3, indicate a variation in the reflected optical power of the trapezoidal slab sensor by approximately 3.5% over the range of 20°C-50°C, with the range of 20°C-25°C only exhibiting a change of approximately 0.5%. It should be noted that these results do nothing to mitigate the effects of moisture on the experimental, which during the course of the water bath experiments was found to significantly impact results.

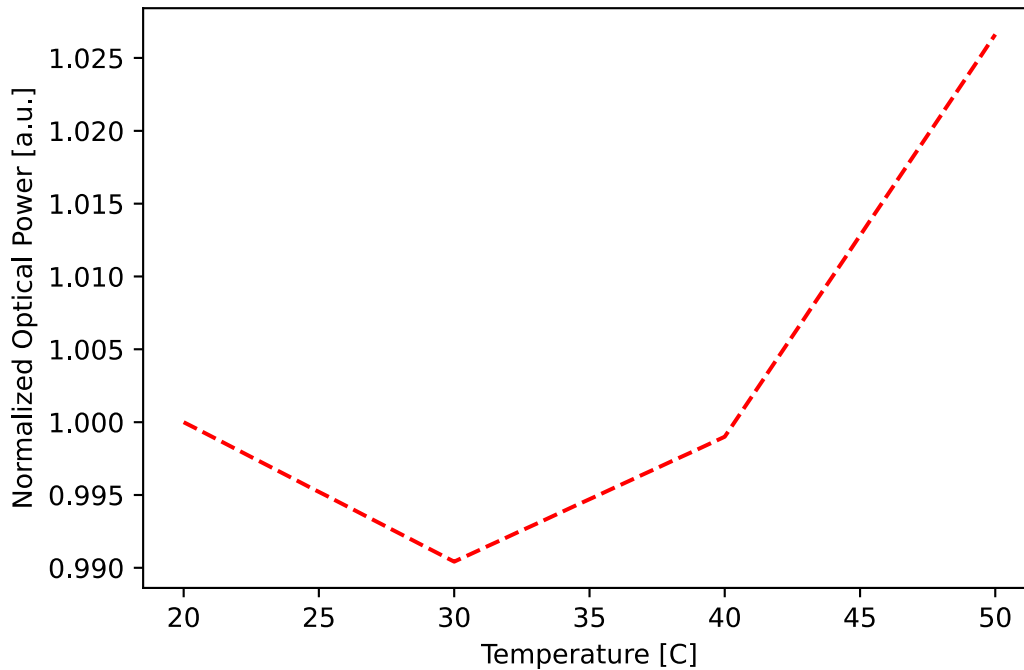


Figure 22: Thermal chamber experimental results - SLED power compensated normalized sensor reflected optical power at steady state temperature for trapezoidal slab

5.3 Water Bath

In an effort to conduct remote thermal experiments with minimal risk of fire, the thermal chamber described in section 5.2.1 was ultimately replaced with a water bath design.

5.3.1 Water Bath Design

The water bath design is composed of the following components as shown in Figure 23:

- Joule Sous Vide (internet enabled immersion cooker/circulator with precise temperature control)
- Water tank
- secondary containment vessel
- Omega HH376 precision resistance temperature detector (RTD) temperature logger
- Custom thermoelectric cooler (TEC)

A small capacity water tank, having a capacity of 9L, was chosen in order to minimize the time required to achieve the set point and to maintain a small enough volume that the integrated water pump of the Joule Sous Vide can adequately mix the water within the tank.

The Joule Sous Vide Internet enabled immersion cooker was chosen due to its low cost, ability to be controlled remotely through Internet, and power rating. The set point of the device is set via mobile application and temperature is maintained by the devices internal controls and feedback. The device has a rated power consumption of 1100W. Given that the specific heat capacity of water is 4184 J/kg/°C and the density of water is 1 kg/L, the device is capable of raising the temperature of the water in the tank at a rate of 1.75 °C/min (neglecting ambient heat loss) when

the water bath is at full capacity. Additionally, the temperature control of the device stated as being capable of ± 0.1 °C accuracy.

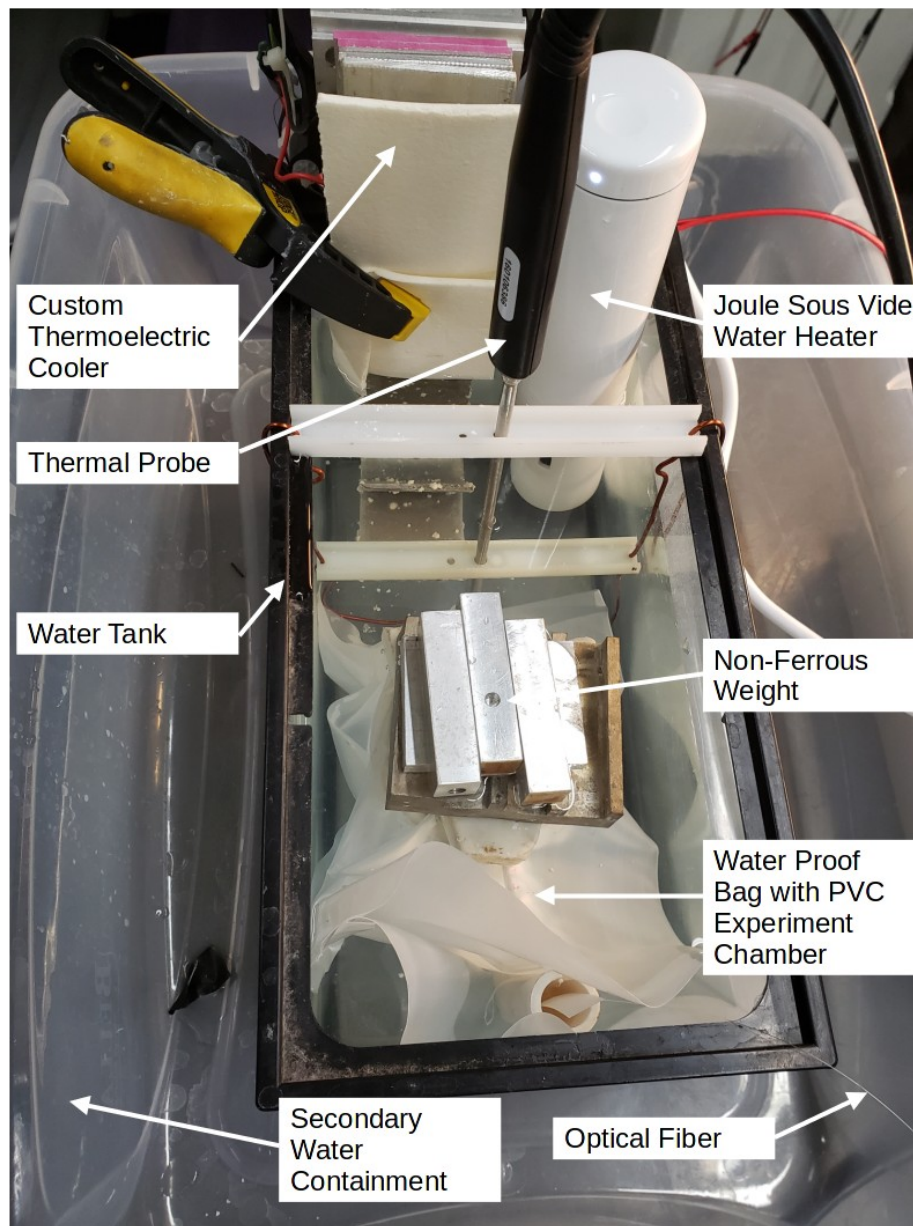


Figure 23: Water bath thermal experiment apparatus (top view)

An Omega HH376 precision RTD temperature logger is used to record the temperature of the water bath via universal serial bus (USB) cable since the Joule Sous Vide does not provide temperature logging capability.

A custom 12V TEC was developed to lower the temperature of the water in the tank in order to extend the low side temperature range of the water bath and accelerate the reduction in water temperature when the set point of the Joule Sous Vide is lowered. The first TEC design iteration consisted of a Peltier module secured with machine screws between a drilled and tapped heat sink and two layers of aluminum bar stock, with thermal paste applied as a thermal interface between the heat sink, Peltier module, and aluminum bar stock. A 12V computer central processing unit (CPU) fan is attached to the heat sink using zip ties to provide air flow to the heat sink and improve cooling efficiency.

The cold side aluminum bar stock sink, having a cross sectional area of 1.6 cm^2 , was able to reduce the temperature of the water bath by approximately 2°C with the impeller of the Joule Sous Vide running. Given the room temperature is typically in the $23\text{-}25^\circ\text{C}$ range, this was not enough to achieve the desired 20°C set point and additional aluminum bar stock was added, bringing the total cross sectional area to 3.2 cm^2 , and reducing the temperature by approximately 4°C with the impeller of the Joule Sous Vide running. The final custom TEC is shown in Figure 24. The block diagram for the cooler is shown in Figure 25. It was subsequently discovered that by turning off Joule Sous Vide, the temperature of the water would reduce by approximately 2°C more and yielding a final temperature in the $17\text{-}19^\circ\text{C}$ range.

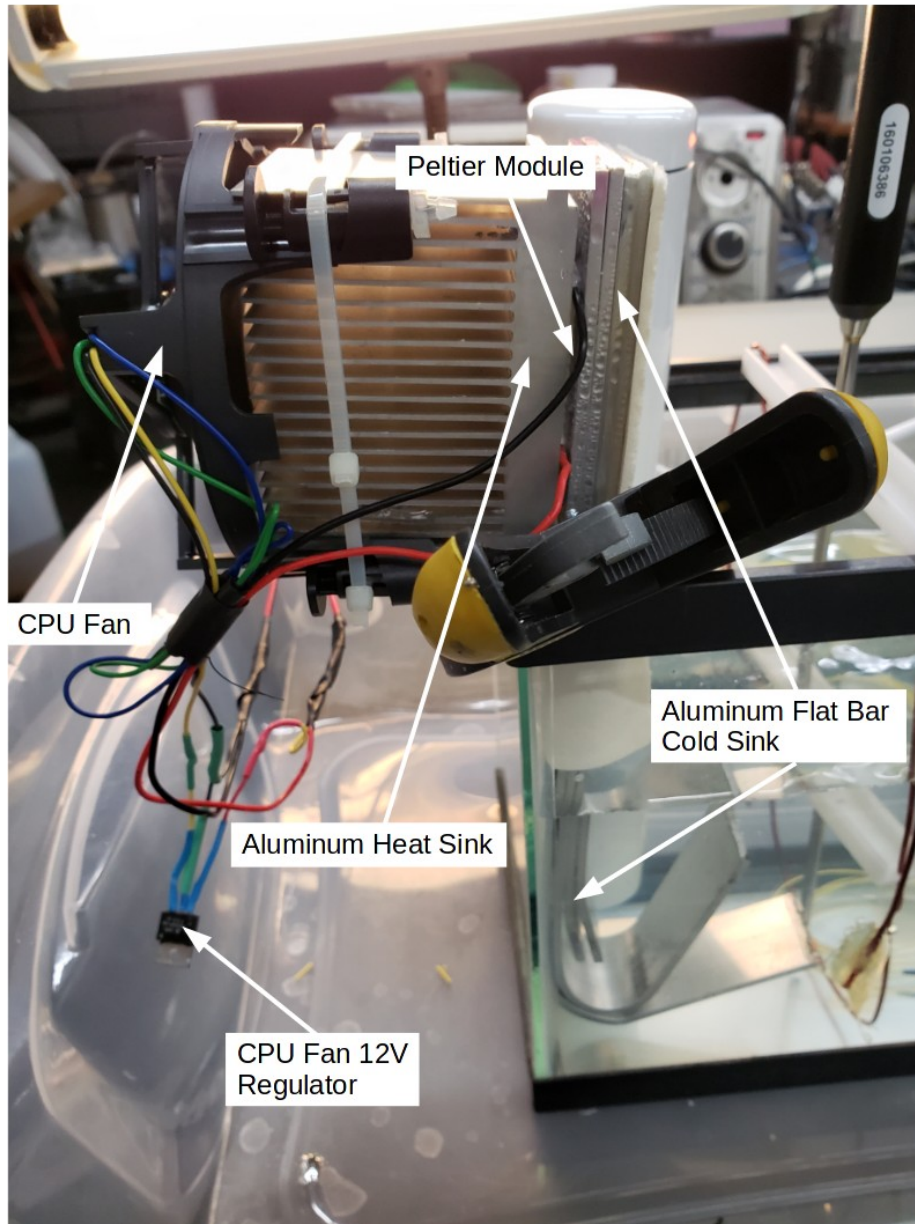


Figure 24: Custom TEC water bath cooler

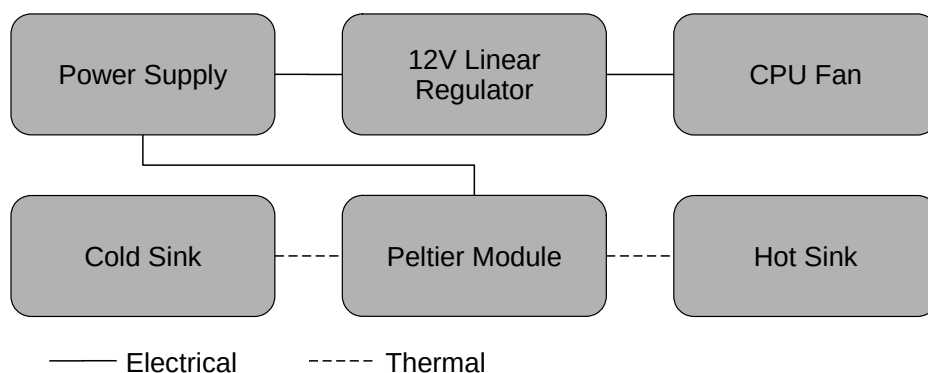


Figure 25: Custom TEC block diagram

5.3.2 Water Bath Experiments

The water bath experimental setup block diagram is shown in Figure 26.

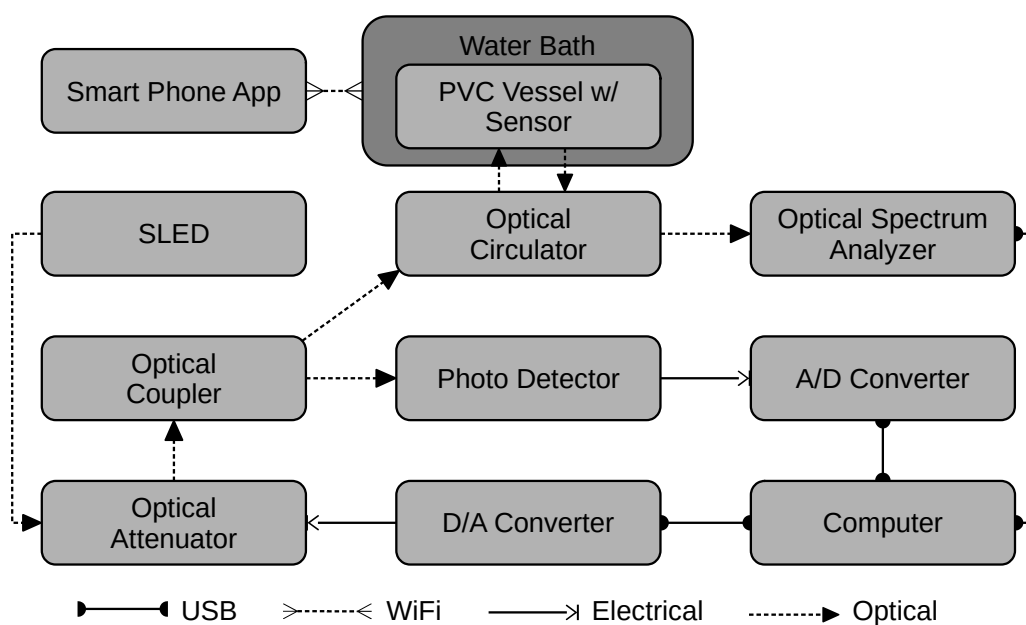


Figure 26: Water bath experimental setup

The water bath experimental setup described in section 5.3.1 was used to gather experimental data to track the effect of temperature on the optical power reflected back in the sensor.

Numerous iterations of the water bath experiment were performed with various methods to immerse the sensor in the water bath. The methods of immersion tried include: 1) direct immersion, 2) immersion in a waterproof bag, 3) immersion in a waterproof bag with the sensor surrounded with desiccant, and 4) sensor placed in a custom polyvinyl chloride (PVC) vessel with lower portion filled with desiccant and placed in a waterproof bag. The reason for the changes came down to the effects of moisture expansion of the composite material, discussed in section 2.5. It was found during direct immersion testing that the peak wavelength of the reflected FBG spectrum was shifted significantly to a longer wavelength when compared to the immersion peak wavelength obtained prior to immersion, indicating that the composite material had expanded during the immersion. Initially, to mitigate this method 2 was tried, but it was found that the moisture content of the sensor still changed over time. method 3 proved better at controlling moisture; however, there were concerns that the weights needed to hold sensor underwater , when surrounded with desiccant, would yield inconsistent results due to the uncontrolled nature of applied mechanical stress to the sensor. The only water bath sensor immersion method that yielded consistent and repeatable results was the custom PVC vessel with the lower portion filled with desiccant and placed in a waterproof bag; therefore, it was the final water bath sensor immersion method chosen.

The water bath thermal experiments, using the custom PVC vessel, consisted of four temperature set points: 20°C, 30°C, 40°C, and 50°C, and two orientations per sensor (0° and 90°). The sensor placements within the PVC vessel are shown in Figure 27.

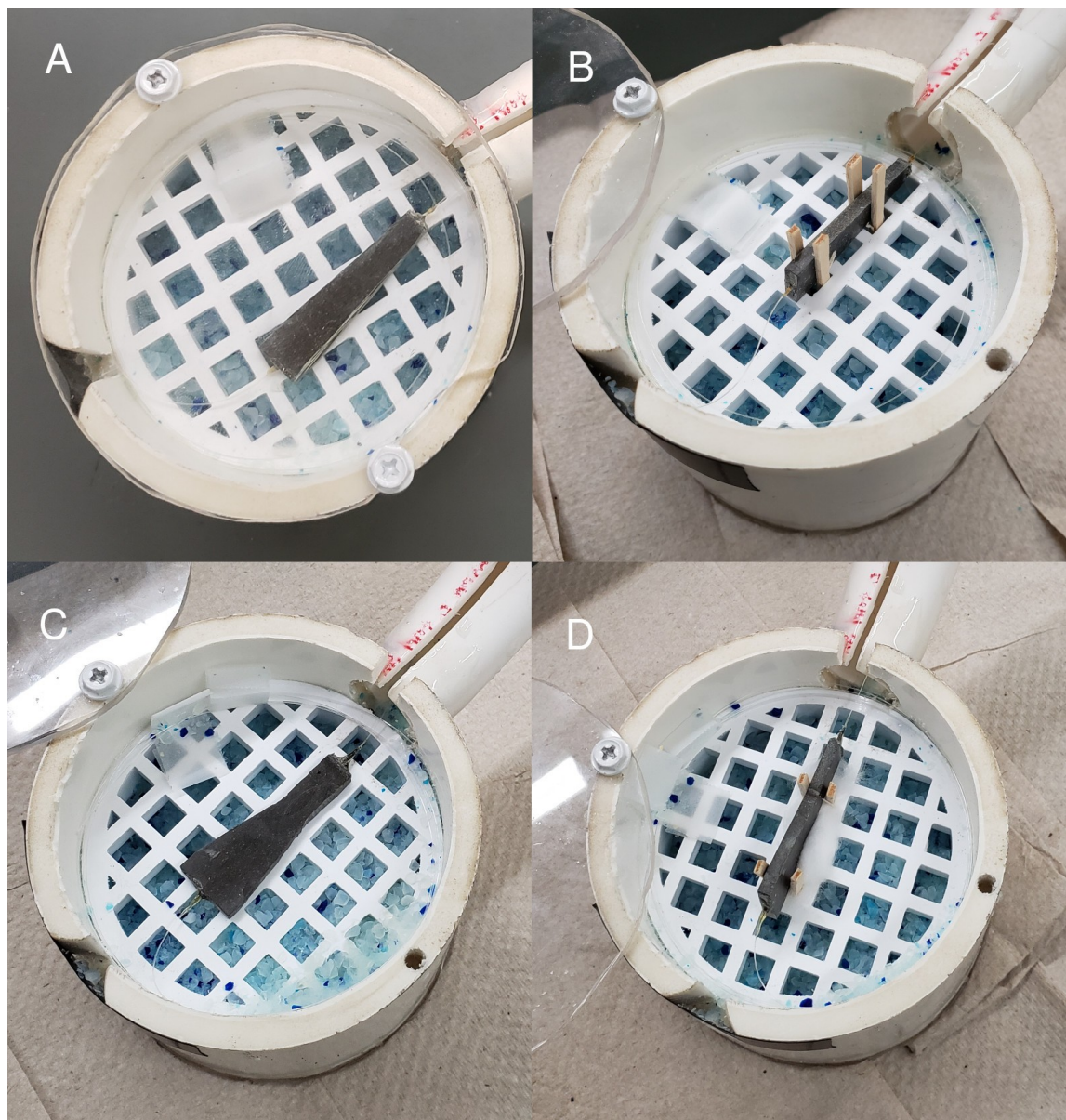


Figure 27: Water bath PVC vessel sensor placement: A) trapezoidal slab 0°, B) trapezoidal slab 90°, C) acute Saccharin quadrilateral 0°, D) acute Saccharin quadrilateral 90°

It was no longer feasible to control the experiment using a single experiment controller like what was done in the thermal chamber experiment described in section 5.2. All temperature changes were done manually in 2 hours increments via the Joule Sous Vide Android application. Additionally, the temperature was set and held at 20°C for 10 minutes prior to the commencement of data collection for the experiments. The original experiment controller program (written in MATLAB script) that was used with the thermal chamber was modified to record only the photodetector voltage to CSV file. The SE-376 program that was supplied with the Omega HH376 Precision RTD Temperature Logger was used to acquire, log, and export to CSV the temperature data for the water bath experiments. The Thorlabs OSA software was used to acquire spectrum data for the sensor in the same manner that was described in section 5.2.1.

5.3.3 Water Bath Data Analysis

Analysis of the water bath experimental data was performed via Python script in a similar manner to that described in section 5.2.3; however, several improvements were made over the original post processing script. The analysis was split between two Python scripts, one to post-process the data and store post-processed data to file, and the second script to generate plots of the data.

Table 4 shows the naming convention used to identify plots in the figures generated during post-processing.

Plot Label	Experimental Configuration
EXP 17	Experiment 17 - Trapezoidal Slab 0°
EXP 18	Experiment 18 - Trapezoidal Slab 0°
EXP 19	Experiment 19 - Trapezoidal Slab 0°
EXP 20	Experiment 20 - Trapezoidal Slab 0°
EXP 21	Experiment 21 - Trapezoidal Slab 90°
EXP 22	Experiment 22 - Trapezoidal Slab 90°
EXP 24	Experiment 24 - Acute Saccharin Quadrilateral Slab 0°
EXP 26	Experiment 26 - Acute Saccharin Quadrilateral Slab 0°
EXP 27	Experiment 27 - Acute Saccharin Quadrilateral Slab 0°
EXP 28	Experiment 28 - Acute Saccharin Quadrilateral Slab 0°
EXP 29	Experiment 29 - Acute Saccharin Quadrilateral Slab 90°
EXP 30	Experiment 30 - Acute Saccharin Quadrilateral Slab 90°
EXP 31	Experiment 31 - Acute Saccharin Quadrilateral Slab 90°

Table 4: Water bath experiment plot naming convention

It should be noted that water bath experiments leading up to the use of the custom PVC vessel are not presented in this thesis and an additional two experiments taken using the custom PVC vessel were eliminated. The data sets eliminated using the PVC vessel are experiments 23 and 25. Experiment 23 data was excluded due to human error resulting in the thermal data not being saved for the experiment. Experiment 25 data was excluded due to the temperature logging software only logging thermal data for only approximately half of the experiment, also caused by human error.

The two main data inputs for this analysis, in addition to the recorded temperature data shown in Figure 28, are the SLED photodetector voltages and sensor reflected optical power calculated from the Thorlabs OSA spectrum data. The SLED photodetector voltages after applying cubic

interpolation to obtain a uniform time step for the experimental data is shown in Figure 29, and the normalized interpolated data is shown in Figure 30. The sensor reflected power after applying cubic interpolation is shown in Figure 31, and the normalized interpolated data is shown in Figure 32.

The filtering portion was modified from the post-processing described in section 5.2.3. A convolution based windowed moving average was used with a 600 second (10 minute) moving window. The main reason for this change was to improve convergence time for the newly added linear regression algorithm, which was added to more accurately determine the optical coupling factor and data alignment for the time offset between optical spectrum analyzer data and photodetector/thermal data.

The linear regression algorithm developed relies on the Python 'scipy.optimize.fmin' library function (FMIN) that iterates over an ordinary least squares function, with input variables corresponding to the optical coupling coefficient, representing the ratio of optical power from the optical coupler branch to the FBG with respect to the branch to the photodetector (previously assumed to be 1:1 based on the optical coupler datasheet), and the time offset between the data sets. For each iteration of the least squares function, the normalized interpolated source adjusted optical power and the filtered normalized interpolated source adjusted optical power are calculated and the square of the difference is returned to the FMIN function. Once the FMIN function satisfies the built-in tolerance criteria, the values returned, shown in Table 5, are used to compute the final source adjusted optical power and the filtered normalized interpolated source adjusted optical power shown in Figure 33 and Figure 34 respectively.

Experiment	Time Offset [s]	Optical Coupling Coefficient [Unitless]
EXP 17	-1.60	1.030
EXP 18	-0.88	1.032
EXP 19	-0.95	1.037
EXP 20	-2.30	1.037
EXP 21	-1.55	1.040
EXP 22	-1.95	1.039
EXP 24	-1.42	1.042
EXP 26	-1.64	1.043
EXP 27	-1.54	1.044
EXP 28	-1.45	1.044
EXP 29	-1.39	1.042
EXP 30	-0.95	1.043
EXP 31	-1.90	1.044

Table 5: Data alignment time offset and coupling coefficients calculated using linear regression method

The filtered normalized interpolated source adjusted optical power was subsequently used to determine the normalized sensor reflected optical power as a function of temperature. The transitions in the thermal data gathered were used to determine where the temperature set point was changed. The last 30 minutes of the filtered normalized interpolated source adjusted optical power data, at each set point temperature, was used to compute an average normalized interpolated source adjusted optical power for each temperature set point. The four average normalized interpolated source adjusted optical power data points are then re-normalized based on the value of the point computed for 20°C, and are shown in Figure 35.

Results present in Figure 35 show just how moisture can affect the measurements of the thermal response of the sensors. Experiments 17 and 24 are good examples of how moisture affected the experimental results since they were both measurements taken ~24 hours after the sensors were placed in the PVC vessel containing desiccant. After the first experiment, for both sensors, the results shown in Figure 35 become consistent for both the 0° and 90° orientations shown in Figure 27. Once moisture affects were mitigated, it becomes clear that both the trapezoidal slab and acute Saccharin quadrilateral slab showed similar changes with respect to change in temperature in the 20°C-25°C range, while the acute Saccharin quadrilateral slab exhibited a significantly lower change in sensor reflected output power over the full range of temperatures tested.

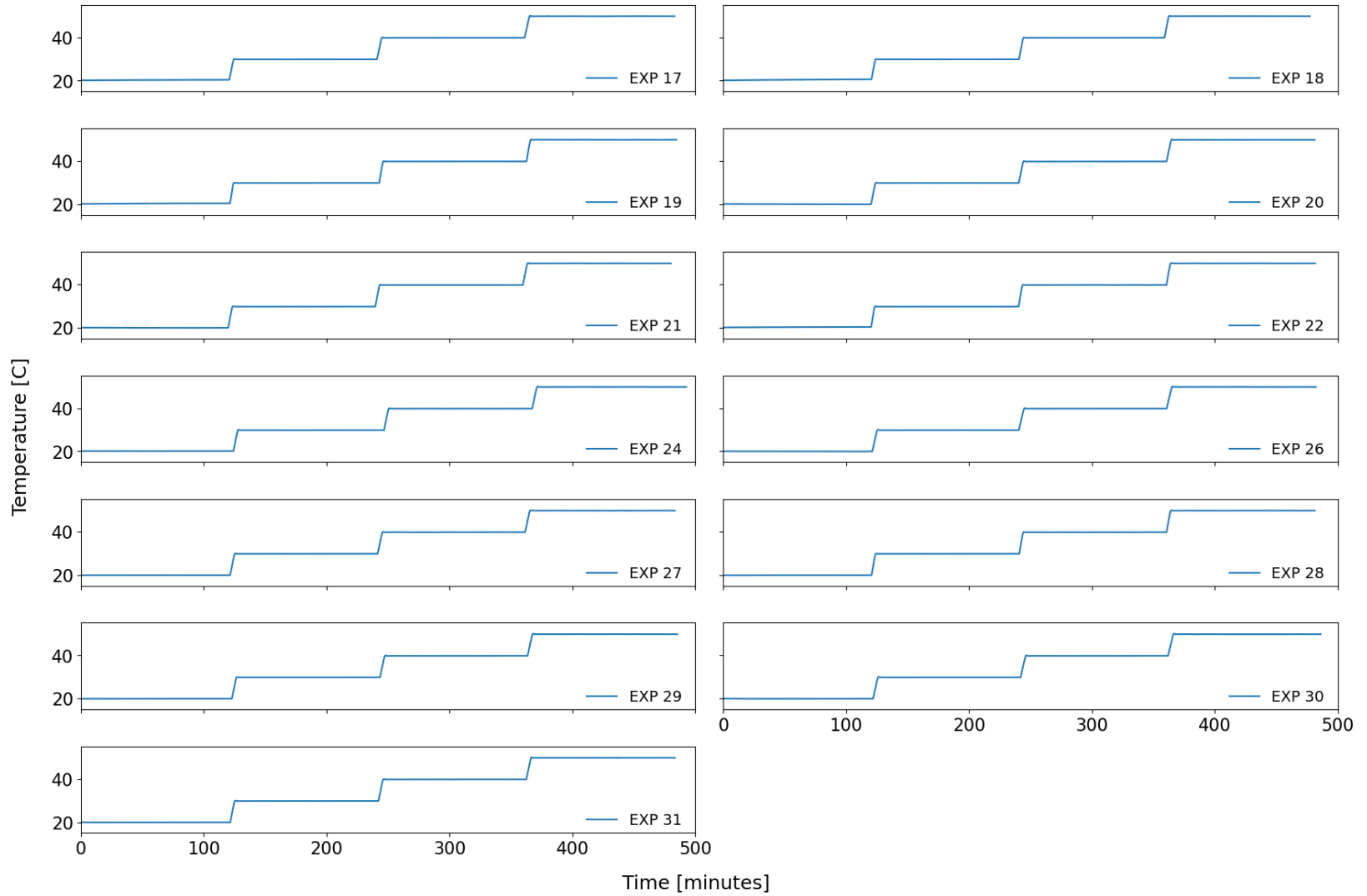


Figure 28: Water bath experimental results - temperature

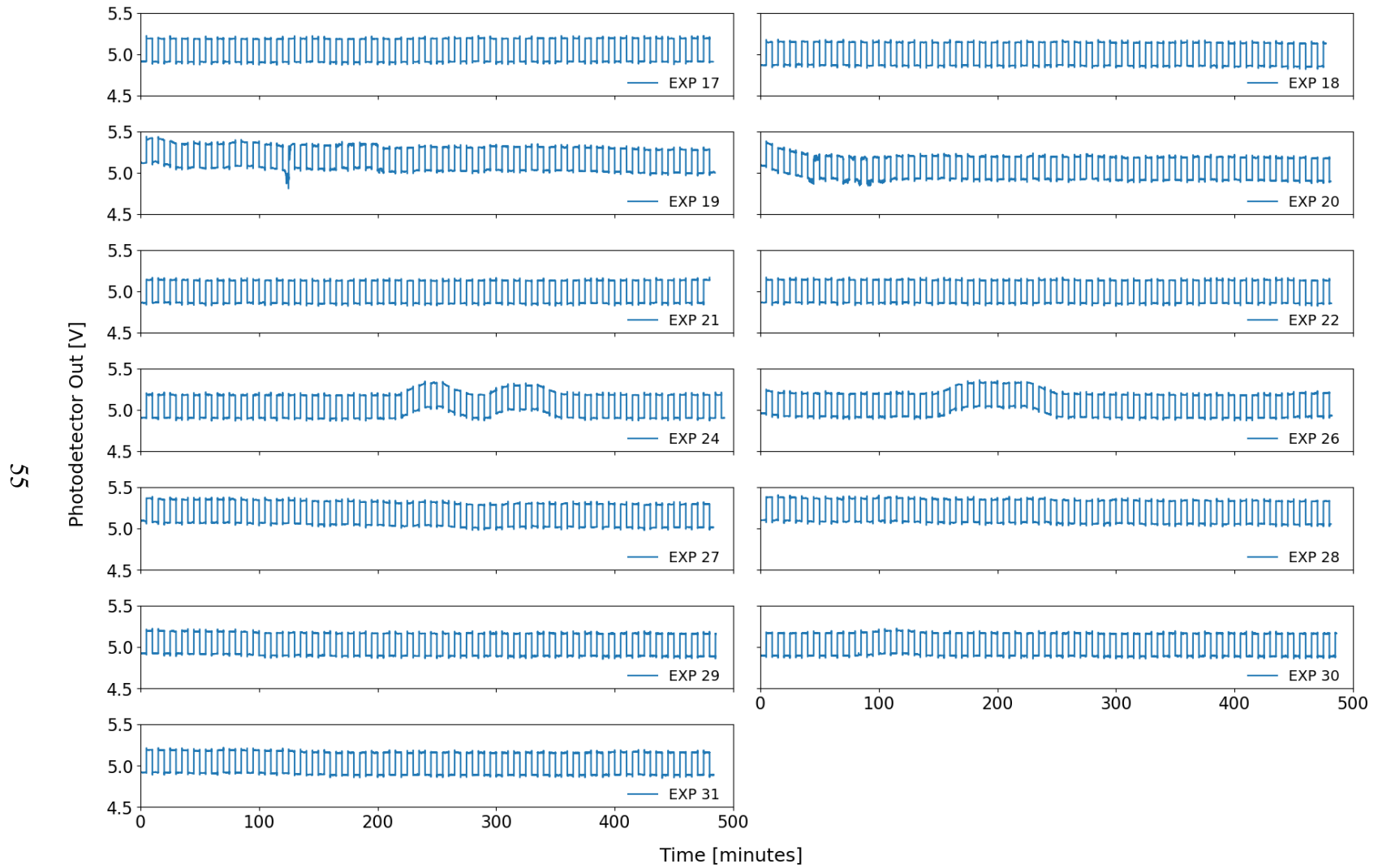


Figure 29: Water bath experimental results - SLED output power measured in terms of photodetector voltage with a 3.8k load resistor - fixed sample time (cubic interpolation)

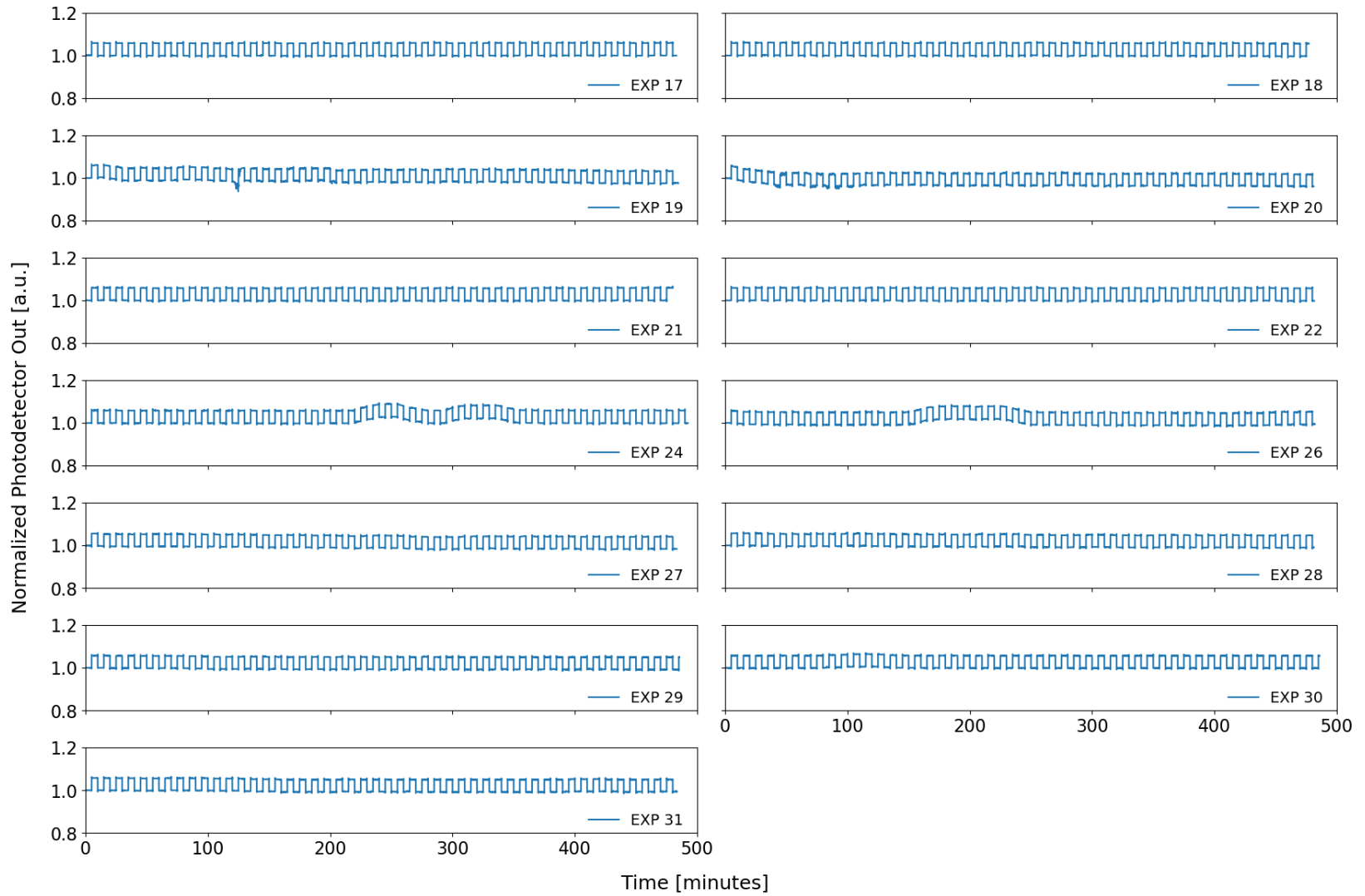


Figure 30: Water bath experimental results - normalized SLED optical power for data in Figure 29

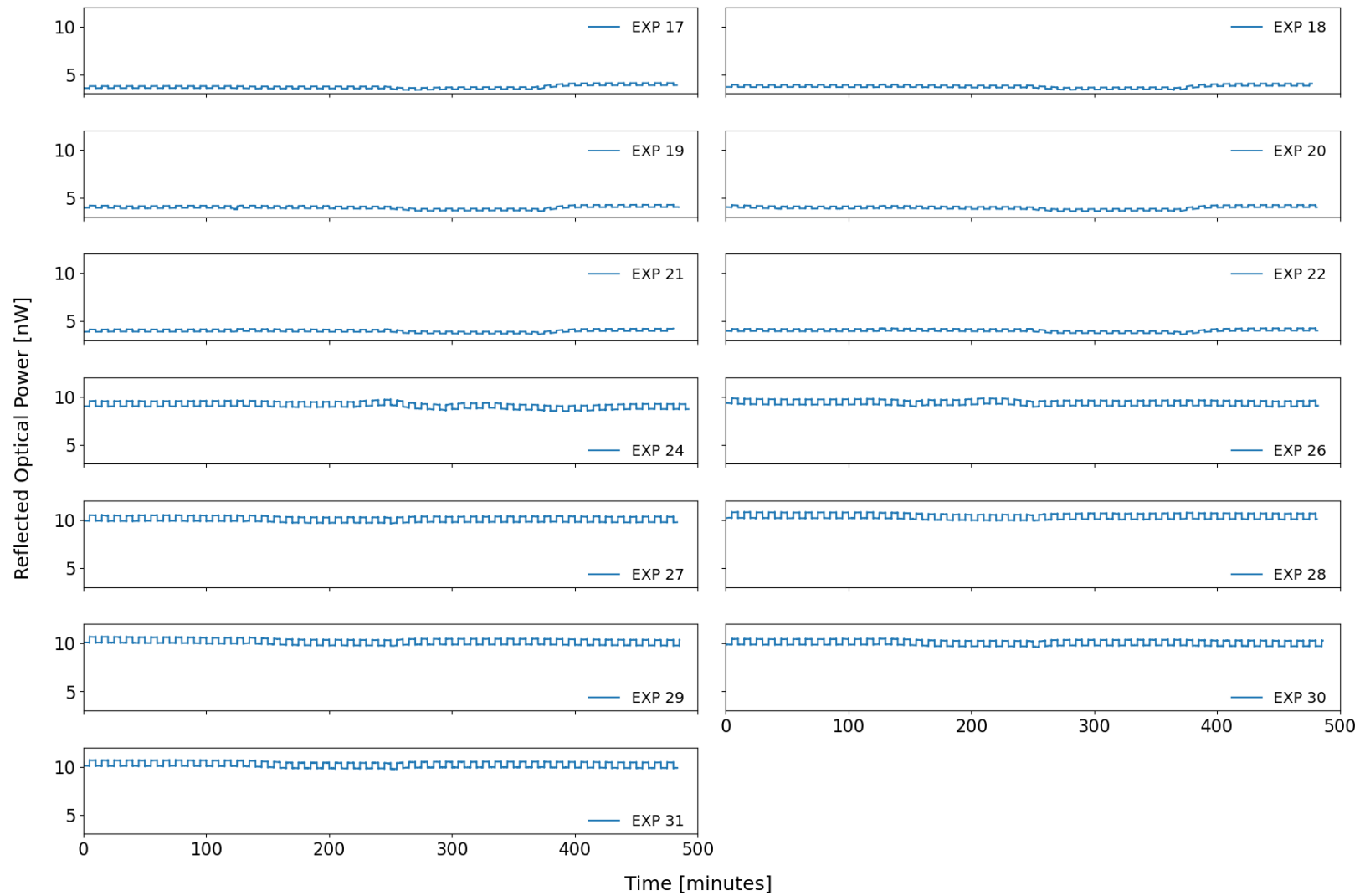


Figure 31: Water bath experimental results - sensor reflected optical power based on integration of OSA spectrum - fixed sample time (cubic interpolation)

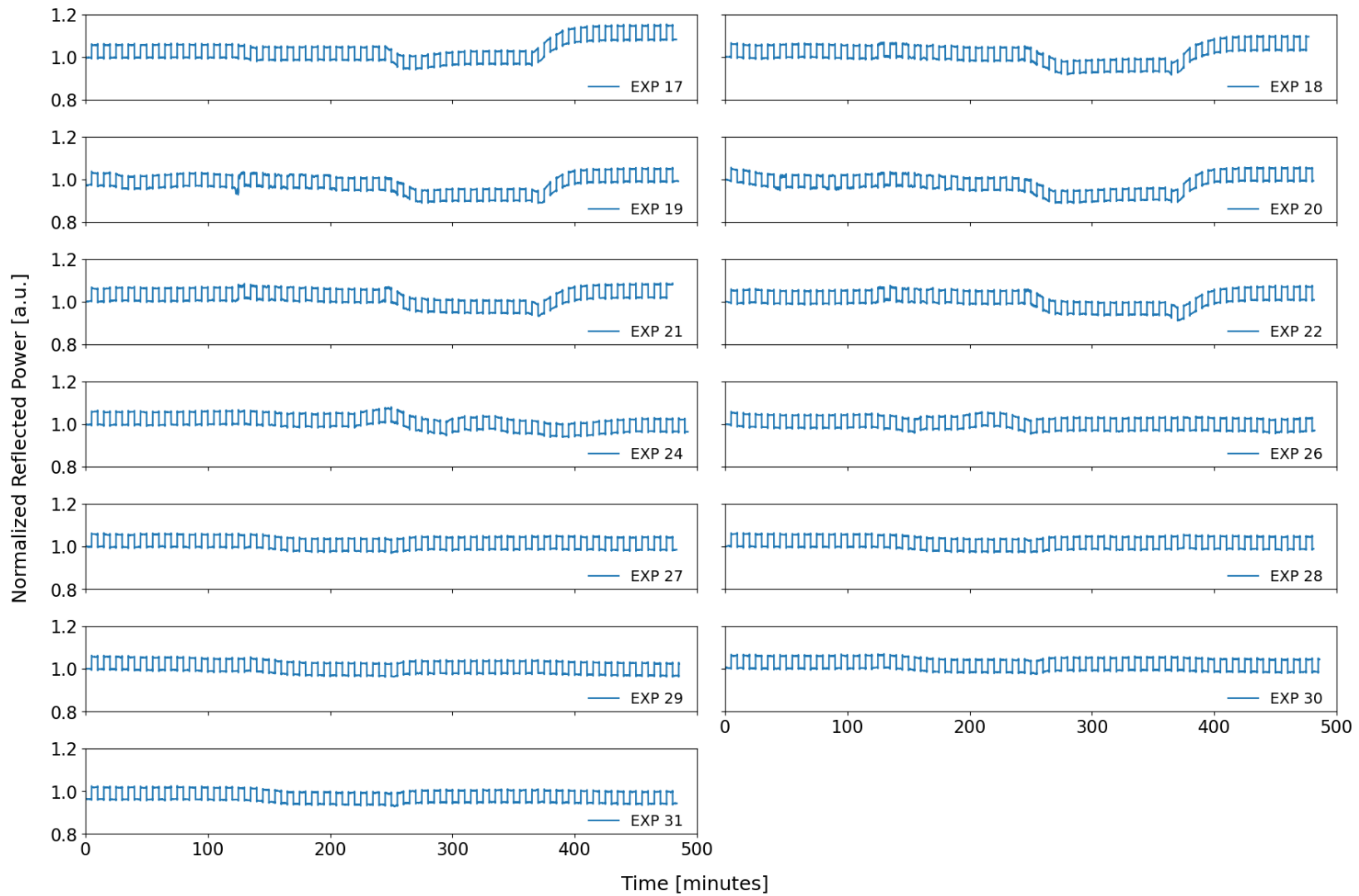


Figure 32: Water bath experimental results - normalized sensor reflected optical power for data in Figure 31

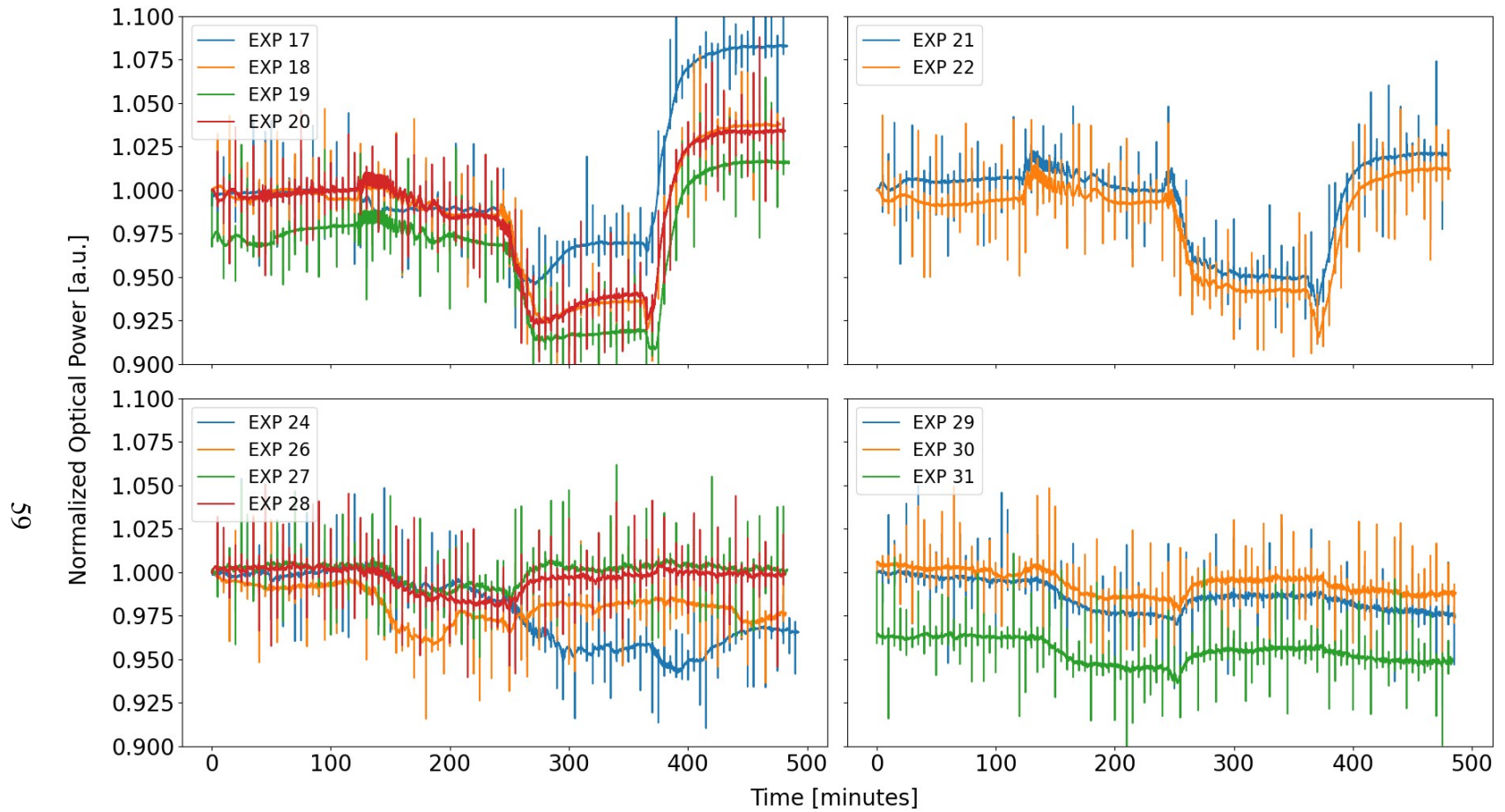


Figure 33: Water bath experimental results - normalized sensor reflected optical power in Figure 32 adjusted for SLED fluctuations with temperature in Figure 30

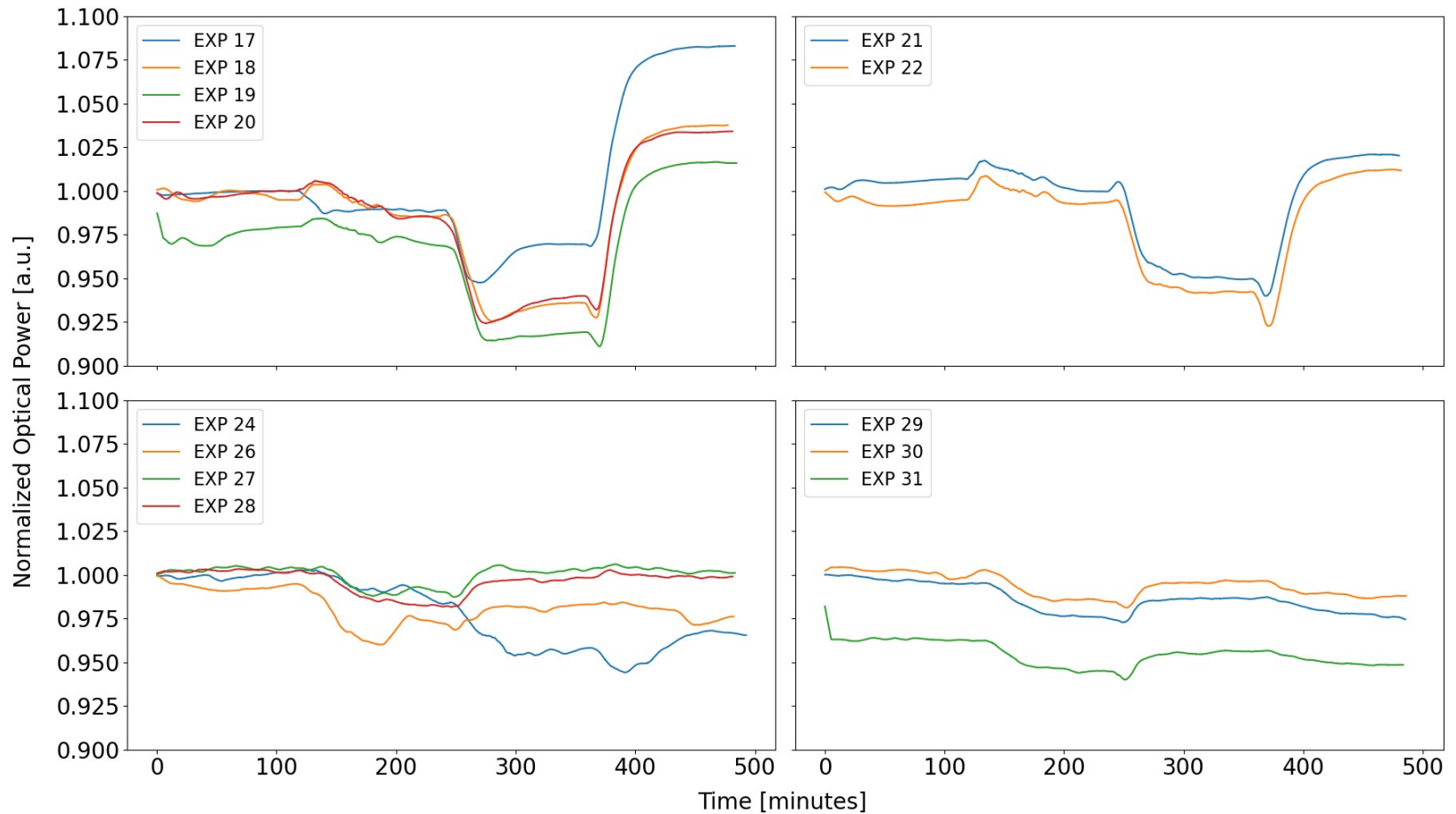


Figure 34: Water bath experimental results - source adjusted normalized sensor reflected optical power in Figure 33 with 10 minute moving average filter applied

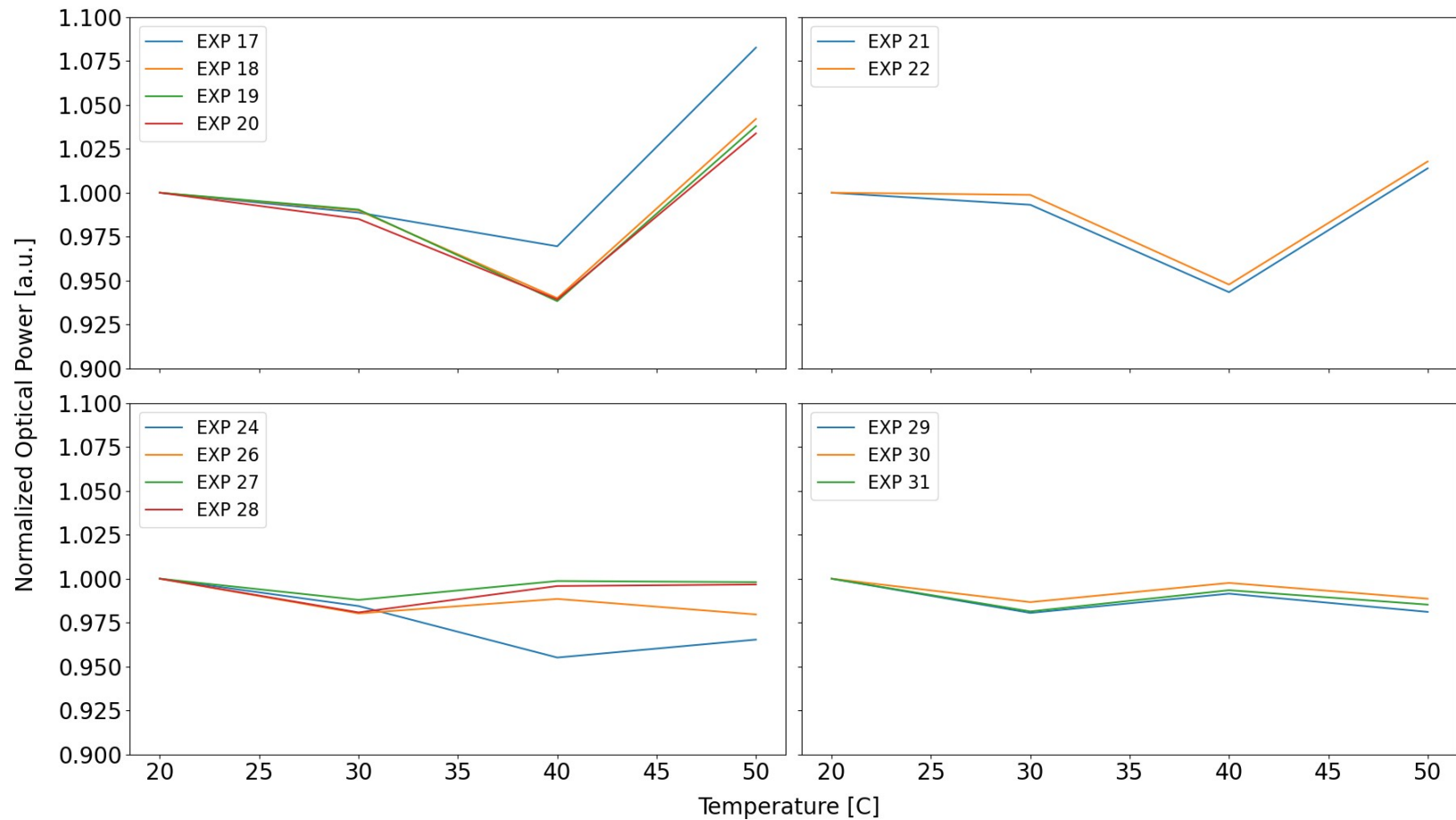


Figure 35: Water bath experimental results - sensor reflected optical power (last 30 minutes hold time average, normalized to 20°C) vs temperature

Chapter 6

6 Conclusion

This thesis presented theory, modeling, hardware design and experimental results, with an emphasis on evaluating the thermal performance, for the trapezoidal slab and acute Saccharin quadrilateral slab magnetostrictive composite sensors for which magnetic characterization was already performed by Frailey [6].

An effort was made to make a fully functioning unified Comsol model capable of simulating both magnetostrictive effects and thermal effects on the sensor. This effort led to the development of equations 12 and 13 in section 2.2 which allowed for the development of a B-H curve for the magnetostrictive composite, for use in Comsol, based on data available through other studies that reported the M-H and λ -H curves. Equation 13 also simplified the mathematics used to calculate magnetostriction in the Comsol modeling. Thermal expansion and select curing effect were added to the model once the magnetostrictive portion of the model was shown to work correctly. This model, in conjunction with Octave scripting, was useful in approximating the coefficient of thermal expansion for the sensor magnetostrictive composite material and indicated that there would be a change in optical power reflected by the sensor due to temperature; however, the model was found to be not so useful in its current state at accurately predicting the reflected optical power of the sensor for thermal modeling. More work is needed to understand the strain induced on the sensor during the curing process due to curing the composite in the presence of a magnetic field and the effects of relative humidity during and after the curing process. Another

issue with a fully unified model is run time. The magnetostriction portion of the model and thermal portion of the model can be solved independently in a fraction of the time it takes to solve them together.

Thermal chamber and water bath test fixtures were designed and developed to support thermal testing of the sensors, with the thermal chamber being replaced with the water bath fixture to support remote thermal testing in a safe manner. The experimental setup was modified from that used in Frailey [6] to compensate for variations in the SLED source and provide more accurate results. Additionally, the new experimental methods that were introduced during the water bath thermal experiments provide the ability to more accurately determine the optical coupling factor for the two branches of the optical circuit following the optical coupler.

During the course of the thermal testing with the water bath method, several susceptibilities that affect both the trapezoidal slab and acute Saccharin quadrilateral slab were uncovered. The first to be discovered was that the sensors are vulnerable to external mechanical forces, owing to the sensitivity of FBGs to mechanical strain, and the result can be impacted by mounting configuration. The second observation was that during the transition between temperature set points, transient effects in the sensor reflected optical power were observed. It was also noted that thermal gradients affected the sensor output and efforts were made while designing the water bath experiments to eliminate this effect as a source of experimental error. Also, it was found that moisture absorbed by the sensors tested affected the thermal response of the sensors tested. This last susceptibility proved most problematic to overcome when experimenting with a water bath. The effect of moisture absorption by the sensor was most obvious when looking at the peak

wavelength of the optical spectrum reflected by the sensors tested when at room temperature, which manifested as a shift to higher wavelength that appeared to be related to the moisture content of the sensor at the time. For this reason, desiccant was introduced to the water bath experiments, and probably should be used in all future experiments with these sensors, to provide a consistent relative humidity for all measurements. Experiments 17 and 24, shown in Figure 35, are good examples of how moisture absorption of the composite material can affected the experimental results.

Once the sensor susceptibilities were identified and mitigated, the results show that acute Saccharin quadrilateral slab exhibited a significantly lower change in sensor reflected output power over the full range of temperatures tested when compared to the trapezoidal slab sensor, especially near the upper bounds of the temperatures tested; however, in the range of 20°C-25°C, both sensors tested exhibited similar thermal responses.

One of the main concerns for this method of sensing following this testing, besides the susceptibilities, is thermal signal to noise ratio when compared to expected response due to applied magnetic field. If for example in the range of 20°C-25°C the sensor response varies by 1% and the maximum response at 300 kA/m applied field is 10%, then the accuracy of the sensor would only have a 10% accuracy over that temperature range, and that is also dependent on successfully and permanently overcoming the other susceptibilities discovered for this sensing method during the experiments performed for this thesis.

Chapter 7

7 Future Work

Future work to perform includes additional modeling and experimental verification of the sensor. One of the more interesting findings during the course of experiments performed was the affect of moisture on the FBG response of the sensor. This effect should be studied in a controlled manner, varying humidity while holding temperature constant, to determine the effects of humidity and obtain an accurate measurement for the CME of the composite material. It would also be interesting to investigate the use of epoxy and composite materials in conjunction with FBGs as a mean of detected humidity.

On the experimental side, it is desirable to perform testing where both the temperature and magnetic field applied to the sensor are both varied and the sensor response observed. This data will provide further insight into whether or not there are any unusual interactions between temperature and applied magnetic field that are yet unknown.

Also, on the experimental side, it would be of interest to determine the affect of a combination of temperature and applied mechanical stress/strain and also study the effects of thermal gradients in a controlled manner. Both have the potential to influence the packaging necessary to ensure more accurate functionality of composite sensors produced in the future.

On the simulation side, combining Comsol simulations to include both magnetic field and thermal expansion physics into a single unified model is desirable to accommodate the simulation

and fine tuning of a geometry of the sensor to maximize the sensitivity of the sensor while minimizing the thermal effects on the sensor, all without having to manufacture and test the sensor until a better design is conceived.

BIBLIOGRAPHY

- [1] *Ansi C84.1-1989 Voltage Rating for Electric Power Systems and Equipment*. Amer Natl Standards Inst.
- [2] M. Aerssens, A. Gusarov, B. Brichard, V. Massaut, P. Megret, and M. Wuilpart, “Faraday effect based optical fiber current sensor for tokamaks,” in *2011 2nd International Conference on Advancements in Nuclear Instrumentation, Measurement Methods and their Applications*, Ghent, Belgium, Jun. 2011, pp. 1–6, doi: 10.1109/ANIMMA.2011.6172868.
- [3] “Disconnecting Circuit Breakers (DCB) with FOCS.” ABB, 2013, [Online]. Available: <http://search-ext.abb.com/library/Download.aspx?DocumentID=1HSM%209543%2021-10en&LanguageCode=en&DocumentPartId=&Action=Launch>.
- [4] J. D. Lopez *et al.*, “Fiber-Optic Current Sensor Based on FBG and Terfenol-D With Magnetic Flux Concentration for Enhanced Sensitivity and Linearity,” *IEEE Sens. J.*, vol. 20, no. 7, pp. 3572–3578, Apr. 2020, doi: 10.1109/JSEN.2019.2959231.
- [5] S. M. Lasassmeh, “Design and Modeling of Fiber Optical Current Sensor Based on Magnetostriction,” Theses and Dissertations, University of Wisconsin-Milwaukee, 2017.
- [6] D. Frailey, “Sensing with Geometry-Dependent Magnetostriction Via an Embedded Fiber Bragg Grating,” Theses and Dissertations, University of Wisconsin-Milwaukee, 2019.
- [7] W. D. Callister and D. G. Rethwisch, *Fundamentals of Materials Science and Engineering: An Integrated Approach*. Hoboken, New Jersey: J. Wiley, 2008.

- [8] J. P. Joule, "On the Effects of Magnetism Upon the Dimensions of Iron and Steel Bars," *Lond. Edinb. Dublin Philos. Mag. J. Sci.*, vol. 30, no. 199, pp. 76–87, Feb. 1847, doi: 10.1080/14786444708645656.
- [9] R. Abbundi and A. E. Clark, "Anomalous Thermal Expansion and Magnetostriction of Single Crystal Terfenol-D," *IEEE Trans. Magn.*, vol. 13, no. 5, pp. 1519–1520, Sep. 1977.
- [10] R. D. James and M. Wuttig, "Magnetostriction of Martensite," *Philos. Mag. A*, vol. 77, no. 5, pp. 1273–1299, Oct. 1998.
- [11] B. D. Cullity and C. D. Graham, *Introduction to Magnetic Materials*, 2nd ed. Hoboken, N.J: IEEE/Wiley, 2009.
- [12] R. A. Kellogg, A. Flatau, A. E. Clark, M. Wun-Fogle, and T. Lograsso, "Quasi-Static Transduction Characterization of Galfenol," in *Aerospace*, Washington, DC, USA, Jan. 2003, pp. 273–280, doi: 10.1115/IMECE2003-43140.
- [13] M. Prabhugoud and K. Peters, "Modified Transfer Matrix Formulation for Bragg Grating Strain Sensors," *J. Light. Technol.*, vol. 22, no. 10, pp. 2302–2309, Oct. 2004, doi: 10.1109/JLT.2004.833281.
- [14] A. Mueller, "Modeling and Experimental Verification of a Fiber Bragg Grating-Based Magnetostrictive Current Sensor," Theses and Dissertations, University of Wisconsin-Milwaukee, 2012.
- [15] R. R. Tummala and A. L. Friedberg, "Thermal Expansion of Composite Materials," p. 5.

- [16] T. A. Duenas and G. P. Carman, "Particle distribution study for low-volume fraction magnetostrictive composites," *J. Appl. Phys.*, vol. 90, no. 5, pp. 2433–2439, Sep. 2001, doi: 10.1063/1.1389518.
- [17] A. Teverovsky, "Environmentally Induced Swelling and Shrinkage of Molding Compounds in PEMs," NEPP 2002, Jan. 2002. Accessed: Aug. 07, 2020. [Online]. Available: <https://nepp.nasa.gov/DocUploads/685BBAF6-425A-4C8A-B625D843DB2A1CC0/Swelling%20and%20Shrinkage%203.doc>.
- [18] Tien-Pei Lee, C. Burrus, and B. Miller, "A Stripe-Geometry Double-Heterostructure Amplified-Spontaneous-Emission (Superluminescent) Diode," *IEEE J. Quantum Electron.*, vol. 9, no. 8, pp. 820–828, Aug. 1973, doi: 10.1109/JQE.1973.1077738.
- [19] G. A. Alphonse, D. B. Gilbert, M. G. Harvey, and M. Ettenberg, "High-Power Superluminescent Diodes," *IEEE J. Quantum Electron.*, vol. 24, no. 12, pp. 2454–2457, Dec. 1988, doi: 10.1109/3.14376.
- [20] O. Levenspiel, "The Three Mechanisms of Heat Transfer: Conduction, Convection, and Radiation," in *Engineering Flow and Heat Exchange*, Boston, MA: Springer US, 1984, pp. 161–188.
- [21] "Thermodynamic Equilibrium."
<https://www.grc.nasa.gov/www/k-12/airplane/thermo0.html> (accessed Nov. 14, 2020).

- [22] L. Khoun and P. Hubert, "Cure Shrinkage Characterization of an Epoxy Resin System by Two in Situ Measurement Methods," *Polym. Compos.*, vol. 31, no. 9, pp. 1603–1610, Sep. 2010, doi: 10.1002/pc.20949.
- [23] C. Y. Lo, S. W. Or, and H. L. W. Chan, "Large Magnetostriction in Epoxy-Bonded Terfenol-D Continuous-Fiber Composite With [112] Crystallographic Orientation," *IEEE Trans. Magn.*, vol. 42, no. 10, pp. 3111–3113, Oct. 2006, doi: 10.1109/TMAG.2006.878873.
- [24] J. J. Liu, Z. B. Pan, X. H. Song, Z. R. Zhang, and W. J. Ren, "Enhanced Magnetostrictive Effect in Epoxy-Bonded $Tb_x Dy_{0.9-x} Nd_{0.1} (Fe_{0.8} Co_{0.2})_{1.93}$ Pseudo 1–3 Particulate Composites," *J. Appl. Phys.*, vol. 117, no. 17, p. 17A914, May 2015, doi: 10.1063/1.4916507.
- [25] A. Rohatgi, "WebPlotDigitizer." <https://apps.automeris.io/wpd/> (accessed Nov. 14, 2020).
- [26] R. E. Jimenez-Mejia, C. T. Law, and R. A. Herrera, "Magnetic Field Sensor Based on a Conical Frustum of Terfenol-D Composite," *IEEE Magn. Lett.*, vol. 10, pp. 1–4, 2019, doi: 10.1109/LMAG.2019.2946366.